arXiv:astro-ph/0107349 v1 18 Jul 2001

ALL-STOKES PARAMETERIZATION OF THE MAIN BEAM AND FIRST SIDELOBE FOR THE ARECIBO RADIO TELESCOPE

Carl Heiles
Astronomy Department, University of California, Berkeley, CA 94720-3411;
cheiles@astron.berkeley.edu

Phil Perillat, Michael Nolan, Duncan Lorimer, Ramesh Bhat, Tapasi Ghosh, Ellen Howell, Murray Lewis, Karen O'Neil, Chris Salter, Snezana Stanimirovic
Arecibo Observatory, Arecibo, PR 00613; email addresses available at *www.naic.edu*

ABSTRACT

Radio astronomical measurements of extended emission require knowledge of the beam shape and response because the measurements need correction for quantities such as beam efficiency and beamwidth. We describe a scheme that characterizes the main beam and sidelobe in all Stokes parameters employing parameters that allow reconstruction of the complete beam patterns and, also, afford an easy way to see how the beam changes with azimuth, zenith angle, and time. For the main beam in Stokes I the parameters include the beam width, ellipticity and its orientation, coma and its orientation, the point-source gain, the integrated gain (or, equivalently, the main beam efficiency); for the other Stokes parameters the beam parameters include beam squint and beam squash. For the first sidelobe ring in Stokes I the parameters include an 8-term Fourier series describing the height, radius, and radial width; for the other Stokes parameters they include only the sidelobe's fractional polarization.

We illustrate the technique by applying it to the Arecibo telescope. The main beam width is smaller and the sidelobe levels higher than for a uniformly-illuminated aperture of the same effective area. These effects are modeled modestly well by a blocked aperture, with the blocked area equal to about 10% of the effective area (this corresponds to 5% physical blockage). In polarized emission, the effects of beam squint (difference in pointing direction between orthogonal polarizations) and squash (difference in beamwidth between orthogonal polarizations) do not correspond to theoretical expectation and are higher than expected; these effects are almost certainly caused by the blockage. The first sidelobe is highly polarized because of blockage. These polarization effects lead to severe contamination of maps of polarized emission by spatial derivatives in brightness temperature.

Subject headings: polarization — instrumentation: polarimeters — techniques: polarimetric — techniques: miscellaneous

1. INTRODUCTION

The Arecibo[1] radio telescope is unique because the feed moves with respect to a reflector that is fixed with respect to the ground. Thus, the properties of the telescope beam can change in a complicated way as a source is tracked because some components of the beam rotate with the parallactic angle and some don't. For example, the beam is significantly elliptical, and the ellipse rotates with parallactic angle; in contrast, the effects of reflector surface imperfections are fixed on the ground. Disentangling these complicated behaviors is best done by parameterizing the beam: some parameters change in recognizable and physically reasonable ways.

Our efforts were directed towards characterizing all of Arecibo's receivers with the partial intent of establishing a historical record so that the beam patterns could be monitored as future improvements in the telescope structure occur. However, our efforts are also useful for the process of interpreting observational results, and can easily be applied to other telescopes. This paper is a condensed version of Arecibo Technical and Operations Memo 2000-03, which covers all of Arecibo's receivers and with more detail.

We devised a simple and fast observing pattern that provides nearly complete information on the main beam and first sidelobe in all four Stokes parameters. We use the digital crosscorrelation technique to derive the Stokes parameters (Heiles 2001). The pattern consists of four continuously sampled scans oriented every 45° with respect to $(\hat{az}, \hat{za})$ yielding an 8-pointed star-shaped pattern that extends out to three nominal HPBW (Half Power Beamwidths) on each side of the nominal pointing position.

These data allow parameterization of the main beam and first sidelobe as described in the following sections. We begin in §2 by describing the parameterization scheme for Stokes I. §3 describes representative Stokes I results for the main beam parameters. §4 compares those results with a theoretical model of a uniformly-illuminated blocked circular aperture. §5 presents Stokes I results on the first sidelobe. §6 defines and describes the parameters beam squint and squash for the polarized Stokes parameters, presents the polarization of the first sidelobe, and calculates the levels of contamination caused by spatial variations in brightness temperature on maps of polarized emission. §7 presents greyscale images of the beam in all four Stokes parameters.

2. PARAMETERIZATION OF THE STOKES I BEAM

[1]The Arecibo Observatory is part of the National Astronomy and Ionosphere Center, which is operated by Cornell University under a cooperative agreement with the National Science Foundation

2.1. Five Parameters that Describe the Main Beam Shape

We follow Rohlfs and Wilson's (2000) definition of the normalized main-beam power pattern, $P(\theta,\phi)_n = \frac{P(\theta,\phi)}{P_{max}}$. We represent it with five parameters of a two-dimensional Gaussian defining a power pattern with ellipticity and coma. The parameters are the average beamwidth Θ_0, beam ellipticity Θ_1 with an orientation $\phi_{\rm beam}$, and coma $\alpha_{\rm coma}$ with orientation $\phi_{\rm coma}$.

To parameterize the elliptical beam, we take the ratio of major to minor axes to be $\frac{\Theta_0+\Theta_1}{\Theta_0-\Theta_1}$ with the major axis oriented at position angle $\phi_{\rm beam}$, and the beamwidth Θ to vary as

$$\Theta = \Theta_0 + \Theta_1 \cos 2(\phi - \phi_{\rm beam}) \; . \tag{1}$$

where ϕ is the position angle in the (az, za) coordinate system, defined to be zero along the positive azimuth axis and increase towards positive zenith angle (see Figure 1).

We parameterize the coma lobe with a function chosen for analytical convenience; it is not based on a proper derivation. The parameters are the coma strength $\alpha_{\rm coma}$ and its position angle $\phi_{\rm coma}$. We assume that the effect of coma depends only on the projection of θ along the coma direction; this distance is

$$\theta_{\rm coma} = \theta \cos(\phi - \phi_{\rm coma}) \; . \tag{2}$$

The normalized power distribution including parameterized ellipticity and coma is then:

$$P_n = \exp\left[-\frac{\theta^2 \left(1 - \min\{\alpha_{\rm coma} \frac{\theta_{\rm coma}}{\Theta_0}, 0.75\}\right)}{\Theta^2} \right] \tag{3}$$

where θ is the great-circle angular distance of the position from the *true* beam center, equal to $\sqrt{az^2_{\rm offset} + za^2_{\rm offset}}$. The term $\min\{\alpha_{\rm coma} \frac{\theta_{\rm coma}}{\Theta_0}, 0.75\}$ is included to prevent the coma term from unduly distorting the beam far from the center. Note that the beamwidth Θ related to the usual half-power beamwidth by $HPBW = 2(\ln 2)^{1/2}\Theta \approx 1.665\Theta$.

Figure 1 illustrates these quantities with a main beam having severe coma and exaggerated ellipticity. In this example, $\alpha_{\rm coma} = 0.2$, $\phi_{\rm coma} = 22.5°$, $\Theta_0 = 3.4$ arcmin, $\Theta_1 = 1$ arcmin, and $\phi_{\rm beam} = -67.5°$.

2.2. Relating the Beam to the Observation Pattern

When observing the beam shape we must point the telescope to an assumed beam center. The four scans of the observing pattern intersect this assumed beam center, as shown by the

dash-dot lines on Figure 1. The difference between the assumed and actual centers is the pointing offset. Thus, in equation 3,

$$az_{\rm offset} = az_{\rm obs} + \delta az \tag{4a}$$

$$za_{\rm offset} = za_{\rm obs} + \delta za \tag{4b}$$

where $(az_{\rm obs}, za_{\rm obs})$ are the "observed" offsets, that is the ones measured with respect to the assumed center.

2.3. The First Sidelobe in Stokes I

Detailed maps of Arecibo's first sidelobe show some azimuthal structure (i.e., with ϕ on Figure 1) (Heiles 2000). Our observing pattern provides four radial cuts through the beam. We least-squares fit each radial cut with three Gaussians, two weak ones at the beginning and end for the sidelobes and a strong one for the main beam. This yields values of the sidelobe height, center, and width at 8 ϕ's. For each one, e.g. the height, we Fourier transform the 8 values and derive 8 complex Fourier coefficients, only 5 of which are independent because the inputs are real numbers. We reconstruct the sidelobe using N Fourier coefficients, with $N \leq 8$. Using $N < 8$ is not unreasonable because the measurement and Gaussian fitting processes are hardly perfect; it is equivalent to performing a least-squares fit on the 8 ϕ's and deriving fewer coefficients. In practice, we reconstruct the sidelobe with $N = 6$, which is just sufficient to reveal the blockage caused by the equilateral triangle feed support structure, which is a major structural component.

This procedure is complicated in practice. In some cuts the sidelobe is absent or is not well-fit. We test each derived sidelobe Gaussian fit and accept it only if its width is smaller than the nominal $HPBW$ and greater than 0.3 times the nominal $HPBW$. We also require the fractional uncertainty in the derived intensity to be less than 0.45. In cases having no acceptable fit, we take the height equal to zero, and take the center and width equal to the average of all the other acceptable centers and widths for that particular group of cuts.

2.4. Effective Area, On-Axis Gain, and Beam Efficiencies

Again we follow Rohlfs and Wilson (2000) and define the directive gain G as the gain relative to an isotropic radiator for a single polarization. Here we are concerned with treating polarization, for which purpose we must explicitly define the *unsubscripted* directive gain to apply to $\frac{\text{Stokes I}}{2}$; below we will subscript it with a polarization label. Conservation of energy requires that G satisfy the relationship

$$\int\int_{\text{whole sky}} G d\Omega = 4\pi \ . \tag{5}$$

The on-axis point-source directive gain is directly related to the effective area $A_{\rm eff}$ by

$$G_{\rm max} = \frac{4\pi A_{\rm eff}}{\lambda^2} \ , \tag{6}$$

and in practical units of source flux in Jy, area in $\rm m^2$ we have

$$KperJy = 10^{-26} \frac{A_{\rm eff}}{2k_B} \tag{7}$$

or

$$A_{\rm eff} = 2 \times 10^{26} k_B KperJy \tag{8}$$

so, eliminating $A_{\rm eff}$

$$G_{\rm max} = \frac{4\pi(2 \times 10^{26} k_B KperJy)}{\lambda^2} \tag{9}$$

$$= \frac{3.47 \times 10^8 KperJy}{\lambda^2_{\rm cm}} \tag{10}$$

where $\lambda_{\rm cm}$ is the wavelength in cm. Arecibo's theoretical gain, without blockage, is $KperJy \approx 11$, which is equivalent to a uniformly illuminated circular aperture with radius 94 m. The normalized power pattern P_n, which we used above in equation 3, is just

$$P_n = \frac{G}{G_{\rm max}} = 2.89 \times 10^{-9} \frac{G\lambda^2_{\rm cm}}{KperJy} \ , \tag{11}$$

so

$$\int\int_{\rm whole\ sky} P_n d\Omega = 3.62 \times 10^{-8} \frac{\lambda^2_{\rm cm}}{KperJy} \ . \tag{12}$$

The "efficiency" of a portion of the telescope's beam is defined as the integral of its directive gain divided its integral over the whole sky. Thus, using units of $\rm arcmin^2$ for Ω and cm for λ,

$$\eta_{\rm beam} = 2.34 \frac{KperJy}{\lambda^2_{\rm cm}} \int\int_{\rm beam} P_n d\Omega_{\rm arcmin^2} \ . \tag{13}$$

Normally we consider the main beam efficiency, but we can also use the same terminology for the sidelobes. The main beam and first sidelobe integrals are, in principle, expressible analytically by our parameterization scheme; in practice, however, we compute them numerically.

3. REPRESENTATIVE OBSERVED PARAMETER VALUES

Table 1 provides representative observed values for the above-defined parameters for two receivers at Arecibo Observatory, measured during September 2000. Both are point-source feeds used with the new Gregorian three-mirror system. The point-source gain at 430 MHz is close

to that expected for a perfect telescope, while in for the L-band Wide receiver (LBW) the gain decreases with frequency. This is almost certainly a result of irregularities in the main reflector; a program of adjustments is planned for early 2001.

3.1. Main Beam Ellipticity and Coma

Arecibo's beam is elliptical by design; $\phi_{\rm beam}$ should be 90°, meaning that the za beam is larger than the az beam. In practice we find that ϕ_{beam} exhibits systematic departures from 90°, ranging from $\sim 80° \rightarrow 110°$ and does not get noticeably worse with frequency. We believe this is a result of blockage.

In September 2000 Arecibo had a noticeable coma lobe. It gets worse with frequency, with strength $\alpha_{\rm coma}$ rising from about 0.015 to 0.15 from 430 to 4500 MHz (at $za \sim 10°$). The direction $\phi_{\rm coma}$ exhibits no clear systematic departure from being constant as a function of (az, za) or frequency, scattering about $\phi \sim 25°$. This suggests that it is tied to the azimuth arm and therefore probably a result of subreflector misalignment.

4. COMPARISON WITH A THEORETICAL MODEL: A UNIFORMLY-ILLUMINATED CIRCULAR APERTURE HAVING BLOCKAGE

It is instructive to compare Arecibo's beam pattern with a theoretical model. The most convenient is a uniformly-illuminated circular aperture. We will then consider a circular aperture with a central circular blockage. Even though Arecibo's beam is elliptical, it's close enough to circular that the model makes physical sense.

4.1. A Uniformly-Illuminated Unblocked Circular Aperture

In this section we will define and evaluate the theoretical parameters for an unblocked aperture, with which we will compare our corresponding observed parameters. This comparison leads to a profusion of subscripts, and to avoid confusion we will first define those subscripts. The subscript "U" denotes the theoretical result for a uniform illumination pattern. There are two forms of such results. One is obtained directly from the theory beginning with equation 14 below, and this is denoted with the additional subscript "I". The other is an approximate theoretical result obtained by fitting with Gaussians (as we do the observational data) the aforementioned direct theoretical result (subscripted with "I"); this approximation is the one we compare with the data, and has no additional subscript. In addition, the subscripts "MB" and "FS" refer to the main beam and first sidelobe, respectively.

The electric field pattern of an unblocked aperture is

$$F(\sin\theta) = 2\frac{J_1(u)}{u}, \tag{14}$$

where

$$u = \frac{\sin\theta}{(\theta_d/\pi)} \quad \text{and} \quad \theta_d = \lambda/D$$

(Rohlfs and Wilson 2000). The field for a blocked aperture is a suitably-weighted arithmetic combination of different diameters. In principle, the best way to fit this model to the data is to compare the observed and theoretical beam shapes. However, this is not so easy because of Arecibo's elliptical beam. Rather, we examine five parameters. Of these, two are *robust* in the sense that they don't depend on assuming a perfectly smooth reflecting surface for the bowl and, in addition, don't depend on knowing an accurate source flux or a noise diode calibration standard (cal) temperature.

The robust parameters specify only the beam shape using ratios of the first sidelobe and main beam. The peak power in the first sidelobe, as a fraction of the peak of the main beam, is $P_{n,FS,U,I}$; the corresponding quantity for the main beam, $P_{n,MB,U,I}$ is unity by definition. We obtain

$$P_{n,FS,U,I} = 0.0175 \tag{15a}$$

and the ratio of beam efficiencies as defined by equation 13 is

$$\left(\frac{\eta_{FS}}{\eta_{MB}}\right)_{U,I} = 0.0861\ , \tag{15b}$$

Obviously, these two parameters are not independent because, to some extent, they measure the same thing.

In the same way we can compute three *non-robust* parameters,

Half-power beam width:

$$(HPBW)_{U,I} = \ 0.597\frac{\lambda_{cm}}{KperJy^{1/2}}\ \text{arcmin.} \tag{16a}$$

Main beam efficiency:

$$(\eta_{MB})_{U,I} = 0.840\ , \tag{16b}$$

And, combining equations 16b and 15b to get the total efficiency in the main beam and first sidelobe:

$$(\eta_{MB} + \eta_{FS})_{U,I} = 0.840(1 + 0.0861) = 0.912\ . \tag{16c}$$

To calculate $HPBW$ in equation 16a we use diameter $d_{\rm eff} = \sqrt{\frac{4A_{\rm eff}}{\pi}}$ and the $HPBW$ for a uniformly-illuminated aperture, $HPBW = 1.03\frac{\lambda}{d_{\rm eff}}$. For the data, the observed $HPBW$ is derived from the Gaussian fit, and the value expected from the model is derived from the effective area $A_{\rm eff}$, which is in turn derived directly from *KperJy*, namely from observations of calibration sources with known flux using a standard noise diode. This dependence on *KperJy* is what makes these parameters non-robust, because *KperJy* is affected by telescope imperfections (surface roughness and subreflector misalignment), loss in waveguide feeds, errors in source calibrator flux, and errors in noise diode calibration temperature.

Our beam parameterization is done through Gaussian fits to the data, and thus we should compare those fits with Gaussian fits to the ideal uniform illumination pattern. Gaussian fits don't represent the theoretical model perfectly, but we can compute correction factors P_{FS}, E_{FS}, and E_{MB}, and H for the Gaussian fits to the ideal uniform circular aperture. As we described above, the Gaussian-fit derived parameters are subscripted only with "U". These correction factors are

$$H = \frac{HPBW_U}{HPBW_{U,I}} \tag{17a}$$

$$E_{MB} = \frac{\eta_{MB,U}}{\eta_{MB,U,I}} \tag{17b}$$

$$E_{FS} = \frac{\eta_{FS,U}}{\eta_{FS,U,I}} \tag{17c}$$

$$P_{FS} = \left(\frac{P_{n,FS,U}}{P_{n,FS,U,I}}\right) . \tag{17d}$$

For example, multiplication of the ideal $HPBW_{U,I}$ by H gives $HPBW_U$, the value that is derived from a Gaussian fit to the ideal beam shape; the factor 0.597 in equation 16a is multiplied by 0.961, becoming 0.574. The ideal beam is wider at the top and falls more rapidly than the Gaussian; this makes $H < 1$ for a uniformly-illuminated aperture with no blocking.

Below, in §4.3, we will consider the effects of blockage. There are corresponding correction factors for blockage, which we quote here for convenience. Table 2 gives values of the (H, P, E) factors in equation 17 for the unblocked case (0%) and for two different blocked cases with 10% and 20% blockage. Empirically, the factors change slowly with blockage, so that these few tabular entries are sufficient.

4.2. Comparison of Observations with the Unblocked Aperture

Table 3 compares some of the observed parameters with those predicted for an unblocked aperture (equations 15 and 16). Arecibo's beam doesn't agree at all with these values. In particular, consider the two robust parameters $P_{n,FS,U}$ and $\left(\frac{\eta_{FS}}{\eta_{MB}}\right)_U$. The observed values are

higher than the unblocked values by factors ~ 2.2 and 4.6, respectively. Conventional feeds, including those used here, produce a tapered illumination, which *decreases* the sidelobe level relative to the uniformly illuminated case. It is impossible to *increase* the sidelobe level without introducing a relative decrease in the center of the illumination pattern—a donut-like pattern. For Arecibo's Gregorian, this occurs naturally because of blockage of the primary reflector by the central support structure. We can use Table 3 to estimate the fraction of blocked area for LBW.

4.3. The Effects of Blockage

We calculate blockage by subtracting the voltage pattern of a circular blocking aperture from that of the illuminated aperture, taking care to keep the power ratio equal to the area ratio. We keep the effective area constant, because $A_{\rm eff}$ is what our observations provide. We normalize the voltage at the center of the effective area's pattern to unity and plot the above quantities versus $\frac{\text{blocked area}}{\text{effective area}}$ in Figure 2. For comparing with observations we assume that the blocked radiation is scattered into the sky, not absorbed, so that equation 5 holds; this reduces η_{MB} by $\frac{\text{effective area}}{\text{illuminated area}}$ relative to the assumption that the blocked radiation is absorbed. Recall that, according to Babinet's principle, the effect of geometrical blockage is doubled; below we will derive blockage $\sim 10\%$, which corresponds to physical blockage $\sim 5\%$.

Figure 2 exhibits plots of the parameters versus the fractional blocked area. Xs on these plots show the measured quantities; the points are placed vertically using the observed value and horizontally using the curves. Thus, the "derived" blockages $\frac{\text{blocked area}}{\text{effective area}}$ that correspond to the model can be read off of the horizontal axes. For the robust parameters, the blockages lie somewhat below and above 0.10 in the top two frames, respectively. It seems reasonable to adopt a blockage of 0.10 for discussion purposes.

For this particular blockage, Figure 3 exhibits the beam shape and, also, the Gaussian fit. The Gaussian is a reasonably accurate rendition of the theoretical model, but has its faults: it doesn't fall to zero between the main beam and the sidelobe and it doesn't reproduce the details of the shape very well. Then again, neither the Gaussian nor the model fits the data particularly well. In fact, they cannot possibly do so because the sidelobe structure changes with ϕ, while the model is circularly symmetric. An additional limitation of both our parameterization and our model is the neglect of additional sidelobes, which contribute non-trivially to the total beam efficiency.

This model of a uniformly illuminated blocked aperture is useful as an indication of expected properties of the main beam and sidelobes. However, it is limited and inaccurate for the following reasons:

(1) Most feed systems don't provide uniform illumination; rather, the illumination is tapered. Tapering increases $HPBW$ and η_{MB} and decreases sidelobe levels, which is opposite to blockage. Thus, the actual geometrical blockage must be somewhat larger than our adopted 10%. Because these two effects work in opposite directions, we surmise that the relationships among our derived

parameters (such as $HPBW$ and η) remain approximately correct.

(2) As a telescope is pushed to higher frequencies, imperfections in the telescope surface become increasingly important. If these imperfections are random, then they scatter radiation away from the main beam according to the Ruze (1966) formulation and will decrease *KperJy* and all beam efficiencies η. Using this reduced *KperJy* may make equation 16a provide a $HPBW$ that is too large. The ratio of FS to MB should not be affected much unless the correlation lengths of the surface imperfections are large—but, of course, for most telescopes, there *do* exist some large scale correlations.

(3) At higher frequencies, large-scale imperfections in the telescope surface and, also, in the mirror alignment become important for most telescopes. These produce significant changes in near-in sidelobes. These effects decrease *KperJy*, increase $HPBW$, tend to increase the first sidelobe power, and tend to transfer some of the main beam power to near-in sidelobes. We expect $\eta_{MB} + \eta_{FS}$ to decrease, but their power to go primarily into near-in sidelobes so that the antenna temperature for an extended source will not decrease very much. Of course, the detailed behavior is complicated, and in addition small-scale random surface irregularities also become important.

4.4. A More Accurate Determination of Blockage

Equation 16a describes a non-robust relationship between two robust parameters, $HPBW$ and λ; these parameters are robust for frequencies below those where large-scale surface irregularities affect the main beamwidth. This equation is non-robust because it depends on *KperJy*. This particular value of *KperJy* is that for a telescope with perfectly smooth reflecting surfaces and perfect mirror alignment. This value can be calculated by the telescope and feed engineers; we denote it by $KperJy_{ideal}$. It can also be measured at frequencies low enough for the telescope to be regarded as perfect; however, such measurements rely on knowing accurate source fluxes and cal temperatures.

We can observationally determine the blockage by first rewriting equation 16a:

$$\left[\frac{KperJy_{ideal}^{1/2}}{(0.597\beta)}\right] = \frac{\lambda_{cm}}{HPBW_{arcmin}} \ . \tag{18}$$

Here β is a parameter that accounts for the blockage and is given by $\beta = H\left[\frac{HPBW}{(HPBW)_U}\right]$, where H comes from Table 2 and the $HPBW$ ratio from Figure 2. Next we measure $HPBW$; knowing $KperJy_{ideal}$, we obtain the blockage factor β.

In practice, one measures $HPBW$ over a range of wavelengths, using feeds with identical illumination patterns, least-squares fit for $\frac{0.597\beta}{KperJy_{ideal}^{1/2}}$, and calculates β. We obtained results at Arecibo for $\lambda = 6 \rightarrow 70$ cm; the fit is very good and, assuming $KperJy_{ideal} = 10.5$, it yields

$\beta = 0.88$. From Figure 2, this corresponds to about 13% blockage. We believe that the blockage so derived should be accurate, but it does depend on knowing a reliable value for $KperJy_{ideal}$.

5. ϕ STRUCTURE IN THE FIRST SIDELOBE

We introduced the Fourier decomposition of the first sidelobe in section 2.3; we obtained a series with 8 points and we use $N = 6$ to reconstruct the sidelobe. This allows us to reconstruct four Fourier components, numbered zero to three. Figure 4 exhibits the az dependence of these components, and we briefly discuss these data to illustrate the power of this representation, because the (az, za) dependences of these Fourier coefficients reveal their probable production mechanisms.

The average amplitude (the zeroth Fourier component, top panel) seems to increase slightly near transit, which probably reflects the slightly increased blockage that occurs there.

The angles of maximum response ϕ_{max} of the first and third Fourier components exhibit a striking dependence with az: the points follow the slope of the dotted line, meaning that these components are fixed with respect to the ground. The third Fourier component would respond to blockage by the triangle structure, which is a large, major structural entity that supports the feed structure; its az dependence implies that it is doing just that. The interpretation for the first Fourier component is less obvious.

The position angles of the second Fourier component are independent of az, implying that they are fixed with respect to the azimuth arm. This is consistent with the blockage of the azimuth arm, which is a linear structure roughly centered on the illumination pattern and should produce a second Fourier component.

The first and third Fourier components are fixed with respect to the ground, in contrast to the behavior of the coma lobe, which is fixed with respect to the azimuth arm. We conclude that the sidelobe structure and coma lobe are, for the most part, unrelated. We reaffirm this conclusion in §6.3, where we discuss the sidelobe polarization.

6. THE POLARIZED STOKES PARAMETERS

One derives the beam structure of the polarized Stokes parameters by observing an unpolarized source, or by subtracting off the polarization of a polarized source to simulate an unpolarized source. An unpolarized source contains power in all polarizations, so beam structure in the polarized Stokes parameters reflects enhanced gain of one polarization over its orthogonal counterpart. Thus, in this section we are discussing the response of the telescope in Stokes Q, U, and V to an unpolarized source. Note that this response, unlike the Stokes I response, can be positive or negative. We assume that the on-axis polarization has been corrected as described in

the companion paper Heiles et al (2001), so that $(Q, U, V) = 0$ at beam center.

6.1. Squint and Squash: Parameters for the Polarized Main Beam

For each polarized Stokes parameter such as Q, we express the response of the main beam with the first two terms of a two-dimensional Taylor expansion. The first derivative term, conventionally called "beam squint", is odd and corresponds to displacement of the beam center in the two orthogonal polarizations. Beam squint is characterized by an angular magnitude and a direction and has a two-lobed structure on the sky, with one positive and one negative lobe. The second term, which we call "beam squash", is even and corresponds to a difference in beam width between the two polarizations. Beam squash is characterized by a magnitude and an orientation and has a four-lobed structure, with lobes on opposite side of beam center having identical signs. We assume that the coma lobe is unpolarized.

To be more precise, consider Stokes Q as an example, which is polarization X minus Y. We define the normalized power pattern for a polarization X as $\frac{G_X}{G_{max}}$.[2] Then the power received from the source in each polarization is

$$P_X = S_X \exp\left[-\frac{\left(\theta + \frac{\delta\theta_Q}{2}\right)^2 \left(1 - \alpha_{\rm coma}\frac{\theta_{\rm coma}}{\Theta_0}\right)}{\left(\Theta + \frac{\delta\Theta_Q}{2}\right)^2}\right] \tag{19a}$$

$$P_Y = S_Y \exp\left[-\frac{\left(\theta - \frac{\delta\theta_Q}{2}\right)^2 \left(1 - \alpha_{\rm coma}\frac{\theta_{\rm coma}}{\Theta_0}\right)}{\left(\Theta - \frac{\delta\Theta_Q}{2}\right)^2}\right] . \tag{19b}$$

where S_X and S_Y are the source fluxes in the two polarizations. Recall that Θ, θ_Q, and Θ_Q all depend on ϕ. The unsubscripted P is the sum (Stokes I), while the difference gives the measured Stokes Q:

$$P_Q = QP_n + \frac{I}{2}\left[\frac{\partial P_n}{\partial\theta_Q}\delta\theta_Q(\phi) + \frac{\partial P_n}{\partial\Theta_Q}\delta\Theta_Q(\phi)\right] . \tag{20}$$

The quantities $\delta\theta_Q(\phi)$ and $\delta\Theta_Q(\phi)$ are not themselves the beam squint and squash. Rather, the squint and squash are represented by (magnitude, position angle), $(\theta_{squint}, \phi_{squint})$ and $(\theta_{squash}, \phi_{squash})$, and are given by

$$\delta\theta_Q = \theta_{squint}\cos(\phi - \phi_{squint}) \tag{21a}$$

[2] Recall that above we defined the unsubscripted G (which includes G_{max}) to apply to $\frac{\text{Stokes I}}{2}$.

$$\delta\Theta_Q = \Theta_{squash} \cos 2(\phi - \phi_{squash}) \ . \tag{21b}$$

The quantity $\delta\theta_Q$ varies as $\cos\phi$ because it is like a pointing offset and has a *direction*. In contrast, the quantity $\delta\Theta_Q$ varies as $\cos 2\phi$: in beam squash, the beamwidth varies as $\cos 2\phi$ so it only has an *orientation*.

6.2. Results for Beam Squint and Squash

We least-squares fit equation 20 to the data, regarding P_n as known. This is acceptable, even though P_n is itself a result of a least-squares fit, because its data are Stokes I with high S/N. We do this in all three polarized Stokes parameters. Figures 5 and 6 show representative plots for Stokes (Q, U). The squint and squash amplitudes are in the few arcsecond range and there is significant variation, but no easily interpretable physical dependence, on (za, az). On the other hand, Stokes V (Figure 7) is more smoothly behaved: the squint is somewhat smaller and maintains a constant ϕ, while the squash is very small.

For the linearly polarized Stokes parameters (Q, U), we expect beam squash but no squint (Tinbergen 1996). The prediction regarding squints is not satisfied at all. Instead, beam squints for Stokes (Q, U) are comparable to that for V. The behaviors of ϕ_{squint} for (Q, U) are uninterpretable in simple terms and provide no hint about the cause of the squint. The beam squash amplitude variations are also uninterpretable. The angles ϕ_{squash} should be fixed with respect to the azimuth arm; very roughly speaking, they are. However, they should differ by 45° between Q and U; they don't.

For Stokes V, one expects beam squint but no beam squash (see discussion by Troland and Heiles 1982). This prediction is reasonably well satisfied. The squint amplitude is roughly constant and its angle ϕ_{squint} is constant, fixed with respect to the azimuth arm as it should be. The squash is small, far smaller than for Stokes (Q, U), although it is not zero.

The reasons for the severe departure of Stokes (Q, U) from theory are completely unclear to us. The absence of a clearly defined dependence with on az suggests a combination of effects that are fixed with respect to the ground and the az arm; the obvious candidates are aperture blockage and secondary/tertiary mirror misalignment.

6.3. Fourier Parameters for the Polarized Sidelobes

For each polarized Stokes parameter such as Q, we follow §5 and express the response of the sidelobe in terms of Fourier components. Figures 8, 9, and 11 display these coefficients for the three polarized Stokes parameters. The zeroth Fourier coefficient describes the net polarization averaged over the sidelobe ring and is shown in the top panels. The first sidelobe is strongly

linearly polarized.

In Stokes Q and U, the first Fourier component dominates and sometimes produces fractional polarizations $\frac{(Q^2+U^2)^{1/2}}{I} \gtrsim 0.5$. Their angles of maximun response ϕ_{max} have a complicated behavior: their slopes with respect to az indicate that they are approximately fixed with respect to the ground, but ϕ_{max} suffers a 180° jump near $az = (-20°, 20°)$ for (Q, U) respectively. The dependences for the second and third Fourier components are even less clear.

Because of the dominance of the first Fourier component, the sidelobe linear polarization has a strong component that is fixed with respect to the ground (apart from the 180° jumps), in contrast to the behavior of the coma lobe, which is fixed with respect to the azimuth arm. Thus we reaffirm the conclusion of §4: the sidelobe structure and coma lobe are, for the most part, unrelated.

The angles shown in Figures 8, 9, and 11 are not the position angles of linear polarization. Rather, they are the angles ϕ, defined in Figure 1, at which the particular Fourier coefficient is maximum. In contrast, Figure 10 exhibits the position angle of linear polarization $PA_{linpol} = 0.5 \tan^{-1} \frac{U}{Q}$ for the four Fourier coefficients. As expected, PA_{linpol} for the zeroth component follows the azimuth arm in its rotation with respect to the sky. For the other components the behavior is more complicated, which occurs because ϕ_{max} changes with azimuth: in other words, the ϕ of maximum response moves around the sidelobe ring differently in Q and U as the azimuth changes, which leads to rotation of PA_{linpol} with respect to the azimuth arm as it rotates when tracking a source.

In Stokes V, the first Fourier component dominates and produces fractional circular polarization $\frac{V}{I} \sim 0.1$. For the first and third Fourier components the angles of maximun response ϕ_{max} are nearly constant, being fixed with respect to the ground. The dependence for the second Fourier components is unclear, perhaps because it is so weak.

6.4. The Effects of Beam Squint and Squash on Extended Sources

Suppose one is observing a large-scale feature where the brightness temperature T_B varies with position. One can express this variation by a two-dimensional Taylor expansion. The first derivative is described by a single term with a magnitude and direction; the second derivative is described by three terms, $\frac{d^2T_B}{daz^2}$, $\frac{d^2T_B}{dza^2}$, $\frac{d^2T_B}{dazdza}$, each of which is an ordinary second derivative with a direction. **In this section and its figures, T_B refers to Stokes I so is twice its conventionally used value**.

Beam squint, by its nature, responds to the first derivative and only slightly to the second; beam squash responds primarily to the second. To illustrate the effects of polarized beam structure, we present plots of the response of the polarized beam to these derivatives. In these plots we adopt derivatives of 1 K arcmin^{-1} and 1 K arcmin^{-2} to facilitate scaling to other

measured derivatives, not because these values are necessarily realistic; also, in these figures the brightness temperatures refer to Stokes I, not $\frac{I}{2}$, so they are twice the conventionally used values. The response comes from three separable causes: main beam squint, main beam squash, and the first sidelobe polarization structure. We show these responses individually and, also, we show the total response.

Figures 12 and 13 show Stokes Q and U. In these two figures, the position angles PA are defined *on the sky with the conventional astronomical definition.* For the first-derivative case, the dominant contribution comes from the first sidelobe, which contributes far more than the main beam squint. The amplitudes are roughly constant with az. The angles of maximum response are, *very* roughly, fixed on the sky (they change less rapidly than az), which is consistent with the first sidelobe's effects being caused by blockage. For the second derivative case, the first sidelobe contribution dominates over main beam squash, but not by much.

Figure 14 shows the Stokes V result. In this figure, PA is the angle of maximum response *defined relative to the azimuth arm.* The total amplitudes for both derivatives are smaller by a factor ~ 10 than for Stokes (Q, U). For the first derivative, the PA is independent of az, as expected from the squint result. The sidelobe is again the dominant contribution, but not overwhelmingly so: in fact, its amplitude is about twice that of the main beam squint but the direction is opposite. This has the curious effect of making the *amplitude* of the total beam response about the same with and without the sidelobe—but reversing the *direction* of gradient for maximum response! For the second derivative, the first sidelobe and main beam squash contribute comparably and the PA behavior is correspondingly complicated.

We emphasize that these particular results can produce serious systematic errors when measuring the polarization of extended emission. The results represented in Figures 12, 13, 14 are contributions in the *polarized* Stokes parameters (Q, U, V) that arise from spatial gradients in the *total intensity* Stokes parameter I. The fractional polarization of extended emission tends to be small, so spatial gradients in I can be very serious. Correcting for them at Arecibo is a complicated business because of the PA variation with (az, za). It is also an uncertain business, especially for (Q, U) and somewhat less so for V, because these variations are unpredictable and must be determined empirically. Presumably, corrections at conventional telescopes are more straightforward.

In that spirit, these plots are more useful as guides of what can be reliably measured at Arecibo than they are for correction of the measurements. Consider, for example, measuring Zeeman splitting of the 21-cm line in emission, which involves measuring Stokes V. Figure 14 shows that a brightness temperature gradient $\frac{dT_B}{d\theta} = 1$ K arcmin^{-1} produces an artificial temperature $V_{\rm art} \sim 0.04$ K response in Stokes V; let this ratio be denoted by $\mathcal{K} \equiv \frac{V_{\rm art}}{dT_B/d\theta} \sim 0.04$ arcmin. Then it's easy to show that, for a Landé g factor 2.8 Hz μG^{-1}, the corresponding artifical magnetic field is $B_{\rm art} = 1690\mathcal{K}\frac{dv}{d\theta}$ μG, where $\frac{dv}{d\theta}$ is the velocity gradient in km s^{-1} arcmin^{-1} and $\mathcal{K}$ is in arcmin. For a representative $\frac{dv}{d\theta} = 1$ km s^{-1} deg^{-1} we get $B_{\rm art} \sim 1.1$ μG. Heiles (1996) presents statistics

of the velocity gradient measured with a 36 arcmin $HPBW$; gradients of 1 km s^{-1} deg^{-1} are not uncommon. Gradients might be larger when measured with smaller $HPBW$. Typical values of B are in the μG range, so this effect can be—but is perhaps not always—serious!

7. IMAGES OF THE BEAM IN ALL STOKES PARAMETERS

Expressing the beam properties in terms of parameters is especially appropriate for quantitative work. However, for getting an intuitive feel for the situation there's nothing like an image. So here we provide images for one of our several hundred beam maps. As with our previous detailed figures, these images are all for LBW (1175 MHz) observing B1749+096; the source was setting near Arecibo's za limit of 20°, with $(az, za) \approx (64°, 18.4°)$.

The main beam parameters are as follows:

For Stokes I, $(\Theta_0, \Theta_1) = (4.00, 0.36)$ arcmin (both are HPBW); $\phi_{\rm beam} = 91.1°$; $\alpha_{\rm coma} = 0.048$; $\phi_{\rm coma} = 41.4°$; mean height of first sidelobe= 0.029.

For Stokes Q, $(\theta_{squint}, \phi_{squint}) = (0.019', -173°)$ and $(\Theta_{squash}, \phi_{squash}) = (0.11', 19°)$. As in Figure 5, Q is oriented 45° to the azimuth arm.

For Stokes U, $(\theta_{squint}, \phi_{squint}) = (0.056', -42°)$ and $(\Theta_{squash}, \phi_{squash}) = (0.061', -47°)$. As in Figure 6, U is aligned with the azimuth arm.

For Stokes V, $(\theta_{squint}, \phi_{squint}) = (0.045', -10°)$ and $(\Theta_{squash}, \phi_{squash}) = (0.007', 37°)$.

The beam is considerably elliptical, which is a result of the high zenith angle. The Stokes Q beam shows the classic four-lobed pattern, beam squash, for linear polarization; in contrast, the U beam is polluted with a large unpredicted squint and a huge linearly polarized sidelobe. Theoretically, the beam squashes in (Q, U) must be aligned with their orientations, and in particular the two four-lobed patterns should be rotated 45° with respect to each other; this is not the case! The V beam is reasonably well-behaved. We commented on these aspects in more detail above.

It is a pleasure to acknowledge insightful and helpful comments by the referee, which substantially improved several aspects of this paper. This work was supported in part by NSF grant 95-30590 to CH.

REFERENCES

Heiles, C. 1996, ApJ, 466, 224.

Heiles, C. 2000, Arecibo Technical and Operations Memo 2000-02.

Heiles, C. 2001, PASP, submitted.

Heiles, C., et al 2001, PASP, submitted.

Rohlfs, K. & Wilson, T.L. 2000, Tools of Radio Astronomy, Springer-Verlag, chapters 5, 6.

Ruze, J. 1966, Proc. IEEE 54, 633.

Tinbergen, J. 1996, Astronomical Polarimetry, CU Press, p. 82.

Troland, T.H. & Heiles, C. ApJ, 252, 179.

This preprint was prepared with the AAS LaTeX macros v4.0.

8. FIGURE CAPTIONS

Fig. 1.— Grey-scale/contour image of a main beam having $\alpha_{\rm coma} = 0.2$, $\phi_{\rm coma} = 22.5^\circ$, $\Theta_0 = 3.4$ arcmin, $\Theta_1 = 1$ arcmin (both Θ's are *HPBW* in this figure), and $\phi_{\rm beam} = -67.5^\circ$. The dashed lines intersect the true beam center; the dashed-dot lines intersect the assumed (from the telescope pointing) beam center, and are the paths of the telescope in the observing pattern. Solid contours are $(0.1, 0.2, \ldots)$ of the peak; dashed contours are $(0.01, 0.02, \ldots)$.

Fig. 2.— Blockage-sensitive, measurable parameters versus the ratio of blocked area to effective area. Solid lines show the parameters as derived by fitting the main beam and first sidelobe to Gaussians; dotted lines show the actual parameters for the theoretical model. The top two frames show the robust parameters of equation 15 and the third and fourth show the non-robust parameters of equation 16.

Fig. 3.— Normalized power pattern P_n, and also the integrand θP_n, for **(1)** the standard model of a uniformly illuminated blocked aperture (solid, dash-dot lines), and **(2)** its Gaussian-fit counterpart (dash, dash-dot-dot-dot lines). The squares and diamonds are representative data points for P_n from the LBW feed at 1415 MHz, obtained by averaging different cuts in one single observing pattern.

Fig. 4.— az dependence of the first four Fourier components of the first sidelobe in Stokes I for LBW at 1175 MHz. The dotted lines correspond to a component being fixed with respect to the ground. Solid lines are amplitude and the points are position angle ϕ_{max}, which is the angle ϕ at which the component peaks (ϕ is defined in Figure 1). For the nth Fourier component ($n = 0 \rightarrow 3$), each point occurs n times over each 360° interval in ϕ, and all of those possibilities are plotted to better clarify the az dependence.

Fig. 5.— (za, az) dependence of amplitudes (in arcmin) and $(\phi_{squint}, \phi_{squash})$ of beam squint and squash for Stokes Q. (Here ϕ is labeled "PA"). The dotted line corresponds to being fixed with respect to the sky or ground. **In this figure, Q is oriented 45° to the azimuth arm and fixed with respect to it.**

Fig. 6.— (za, az) dependence of amplitudes (in arcmin) and $(\phi_{squint}, \phi_{squash})$ of beam squint and squash for Stokes U. (Here ϕ is labeled "PA"). The dotted line corresponds to being fixed with respect to the sky or ground. **In this figure, U is aligned with the azimuth arm and fixed with respect to it.**

Fig. 7.— (za, az) dependence of amplitudes (in arcmin) and $(\phi_{squint}, \phi_{squash})$ of beam squint and squash for Stokes V. (Here ϕ is labeled "PA"). The dotted line corresponds to being fixed with respect to the sky or ground.

Fig. 8.— az dependence of the first four Fourier components of the first sidelobe in Stokes Q for LBW at 1175 MHz. The dotted lines correspond to a component being fixed with respect to the

ground. Solid lines are amplitude and the points are position angle ϕ_{max}, which is the angle ϕ at which the component peaks (ϕ is defined in Figure 1). For the nth Fourier component ($n = 0 \rightarrow 3$), each point occurs n times over each 360° interval in ϕ, and all of those possibilities are plotted to better clarify the az dependence.

Fig. 9.— az dependence of the first four Fourier components of the first sidelobe in Stokes U for LBW at 1175 MHz. The dotted lines correspond to a component being fixed with respect to the ground. Solid lines are amplitude and the points are position angle ϕ_{max}, which is the angle ϕ at which the component peaks (ϕ is defined in Figure 1). For the nth Fourier component ($n = 0 \rightarrow 3$), each point occurs n times over each 360° interval in ϕ, and all of those possibilities are plotted to better clarify the az dependence.

Fig. 10.— az dependence of the position angle of linear polarization PA_{linpol} for the first four Fourier components of the first sidelobe for LBW at 1175 MHz (PA is the conventional astronomical definition). The dotted lines correspond approximately to PA_{linpol} being fixed with respect to the azimuth arm.

Fig. 11.— az dependence of the first four Fourier components of the first sidelobe in Stokes V for LBW at 1175 MHz. The dotted lines correspond to a component being fixed with respect to the ground. Solid lines are amplitude and the points are position angle ϕ_{max}, which is the angle ϕ at which the component peaks (ϕ is defined in Figure 1). For the nth Fourier component ($n = 0 \rightarrow 3$), each point occurs n times over each 360° interval in ϕ, and all of those possibilities are plotted to better clarify the az dependence.

Fig. 12.— az dependence of the telescope's response to the first spatial derivative in brightness temperature (top two panels) and to the second derivative (bottom two panels), all for Stokes Q. PA is direction of maximum response. **In this figure, Q and PA are defined on the sky with the conventional astronomical definition.** T_B refers to Stokes I so is twice is conventionally used value.

Fig. 13.— az dependence of the telescope's response to the first spatial derivative in brightness temperature (top two panels) and to the second derivative (bottom two panels), all for Stokes U. PA is direction of maximum response. **In this figure, U and PA are defined on the sky with the conventional astronomical definition.** T_B refers to Stokes I so is twice is conventionally used value.

Fig. 14.— az dependence of the telescope's response to the first spatial derivative in brightness temperature (top two panels) and to the second derivative (bottom two panels), all for Stokes V. PA is the ϕ of maximum response, **defined relative to the azimuth arm as in Figure 1**. T_B refers to Stokes I so is twice is conventionally used value.

Fig. 15.— Grey-scale/contour of the Stokes I main beam and first sidelobe reconstructed from the derived parameters. Solid contours are $(0.1, 0.2, \ldots)$ of the peak; dashed contours are

$(0.01, 0.02, \ldots)$.

Fig. 16.— Grey-scale/contour of the Stokes Q main beam and first sidelobe reconstructed from the derived parameters. Black contours are for areas with negative Q with the grey scale tending towards white; white contours are positive Q with the greyscale tending towards black. Contours are in percent of Stokes I at beam center and spaced by 0.4%; the 0% contour is omitted. As in Figure 5, Q is oriented 45° to the azimuth arm.

Fig. 17.— Grey-scale/contour of the Stokes U main beam and first sidelobe reconstructed from the derived parameters. Black contours are for areas with negative U with the grey scale tending towards white; white contours are positive U with the greyscale tending towards black. Contours are in percent of Stokes I at beam center and spaced by 0.4%; the 0% contour is omitted. As in Figure 6, U is aligned with the azimuth arm.

Fig. 18.— Grey-scale/contour of the Stokes V main beam and first sidelobe reconstructed from the derived parameters. Black contours are for areas with negative V with the grey scale tending towards white; white contours are positive V with the greyscale tending towards black. Contours are in percent of Stokes I at beam center and spaced by 0.2%; the 0% contour is omitted.

Table 1. REPRESENTATIVE OBSERVED PARAMETER VALUES

RCVR	FREQ	SOURCE	za	$P_{n\,,FS}$	$\frac{\eta_{FS}}{\eta_{MB}}$	$KperJy$	$HPBW$	η_{MB}	$\eta_{MB}+\eta_{FS}$
430G	430	B1634+269	10	.039	0.33	10.3	10.9	0.66	0.88
LBW	1175	B1634+269	10	.043	0.32	8.7	4.0	0.56	0.75
LBW	1415	B1634+269	10	.046	0.32	7.5	3.4	0.50	0.67
LBW	1666	B1634+269	10	.042	0.31	6.9	2.9	0.48	0.62

Note. — za is in degrees and $HPBW$ is in arcmin.

Table 2. FACTORS IN EQUATIONS 17 VERSUS BLOCKAGE

FACTOR	0%	10%	20%
H	0.961	0.955	0.952
P_{FS}	1.038	1.038	1.033
E_{MB}	1.060	1.067	1.070
E_{FS}	0.865	0.925	0.947

Table 3. COMPARISON OF OBSERVED AND UNBLOCKED MODEL PARAMETERS

RCVR	FREQ	$\frac{P_{FS}}{(P_{FS})_U}$	$\frac{(\eta_{FS}/\eta_{MB})}{(\eta_{FS}/\eta_{MB})_U}$	$d_{\rm eff}$	$\frac{HPBW}{(HPBW)_U}$	$\frac{\eta_{MB}}{(\eta_{MB})_U}$	$\frac{\eta_{MB}+\eta_{FS}}{(\eta_{MB}+\eta_{FS})_U}$
430G	430	2.2	4.7	190	0.87	0.74	0.92
LBW	1175	2.4	4.6	175	0.80	0.63	0.79
LBW	1415	2.5	4.6	162	0.75	0.56	0.70
LBW	1666	2.3	4.4	156	0.71	0.54	0.65

Note. — See §4 for parameter definitions. $d_{\rm eff}$ is in meters.

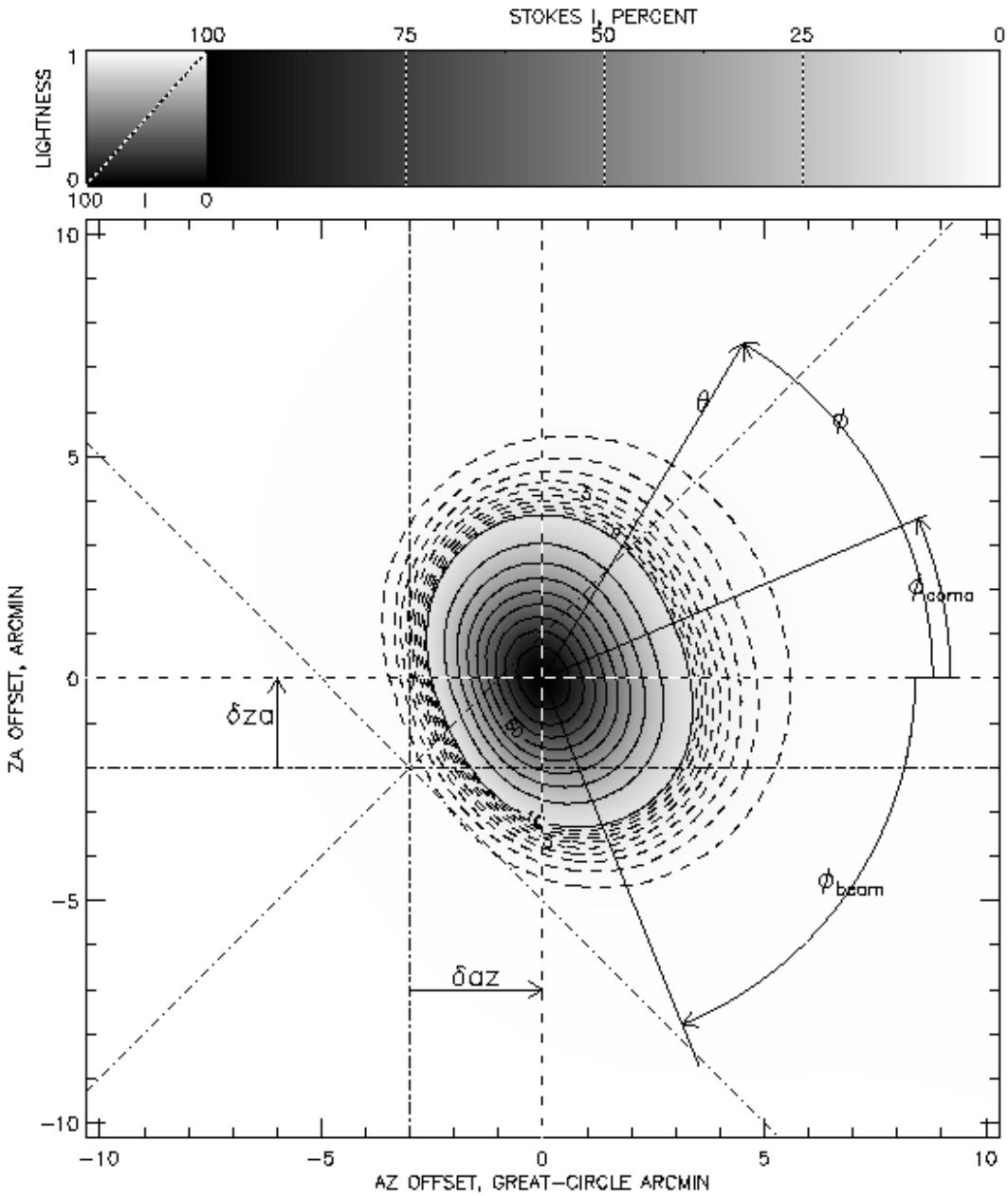
STOKES I, PERCENT
100
75
50
25
0
LIGHTNESS
1
0
100
I
0
10
5
0
−5
−10
ZA OFFSET, ARCMIN
AZ OFFSET, GREAT−CIRCLE ARCMIN
−10
−5
0
5
10
θ
ϕ
ϕcorma
ϕbeam
δza
δaz

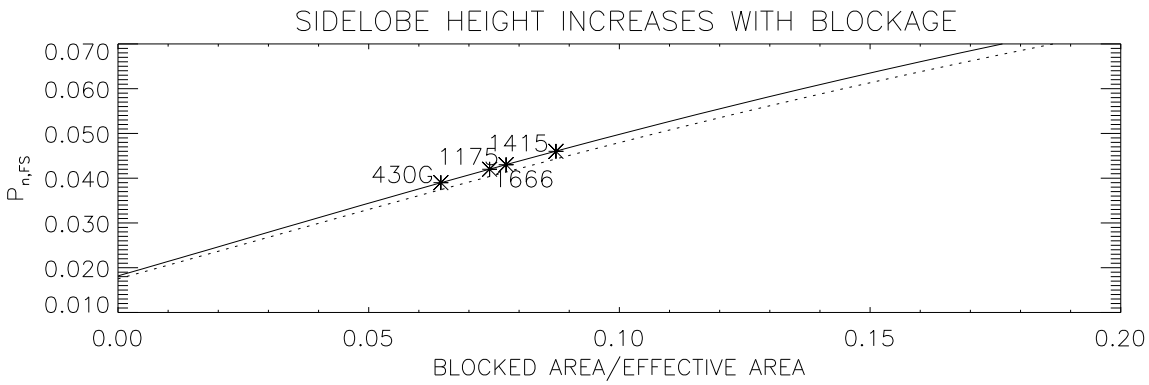
SIDELOBE HEIGHT INCREASES WITH BLOCKAGE
0.070
0.060
0.050
0.040
0.030
0.020
0.010
$P_{n,FS}$
1415
1175
430G
1666
0.00
0.05
0.10
0.15
0.20
BLOCKED AREA/EFFECTIVE AREA

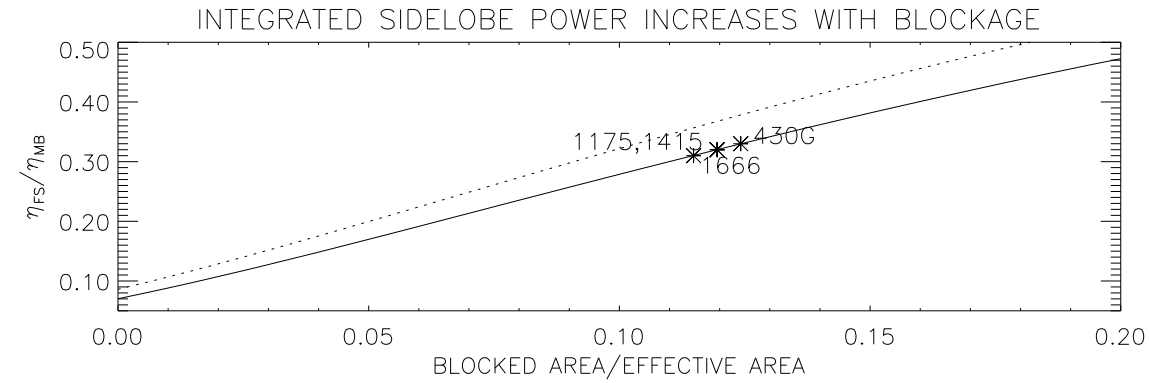
INTEGRATED SIDELOBE POWER INCREASES WITH BLOCKAGE
0.50
0.40
0.30
0.20
0.10
η_{FS}/η_{MB}
1175,1415
430G
1666
0.00
0.05
0.10
0.15
0.20
BLOCKED AREA/EFFECTIVE AREA

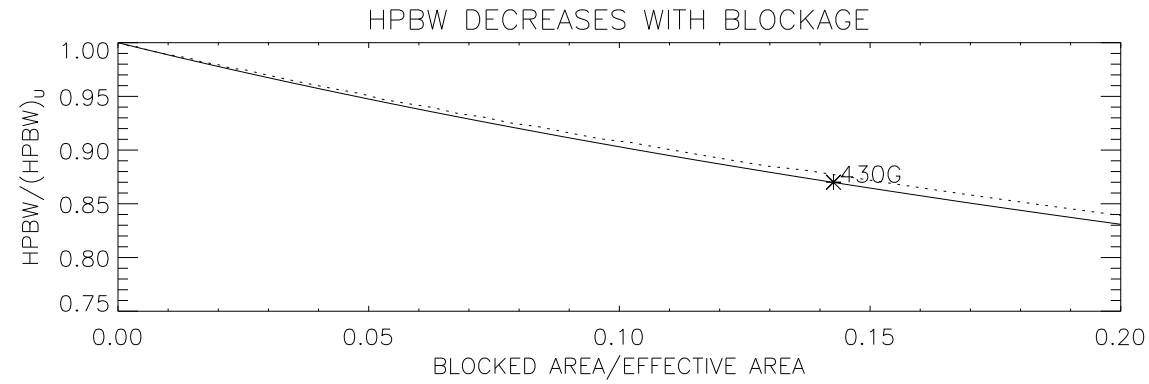
HPBW DECREASES WITH BLOCKAGE
1.00
0.95
0.90
0.85
0.80
0.75
$HPBW/(HPBW)_U$
430G
0.00
0.05
0.10
0.15
0.20
BLOCKED AREA/EFFECTIVE AREA

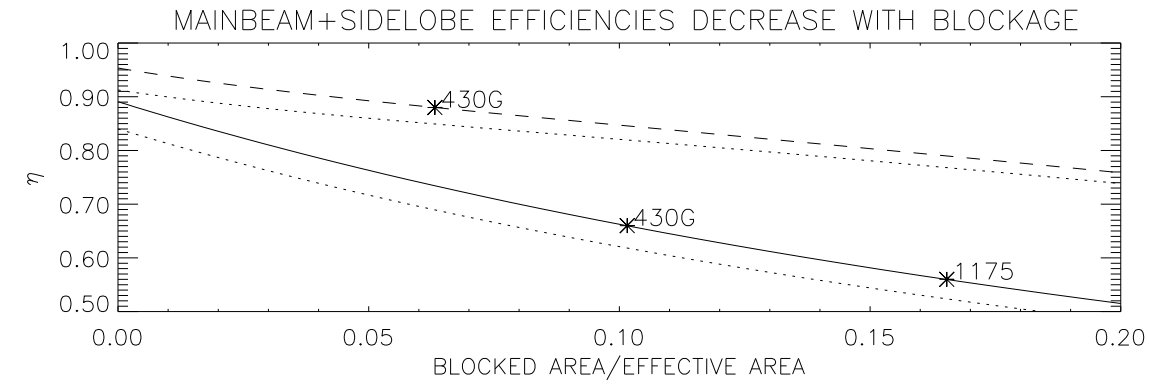
MAINBEAM+SIDELOBE EFFICIENCIES DECREASE WITH BLOCKAGE
1.00
0.90
0.80
0.70
0.60
0.50
η
430G
430G
1175
0.00
0.05
0.10
0.15
0.20
BLOCKED AREA/EFFECTIVE AREA

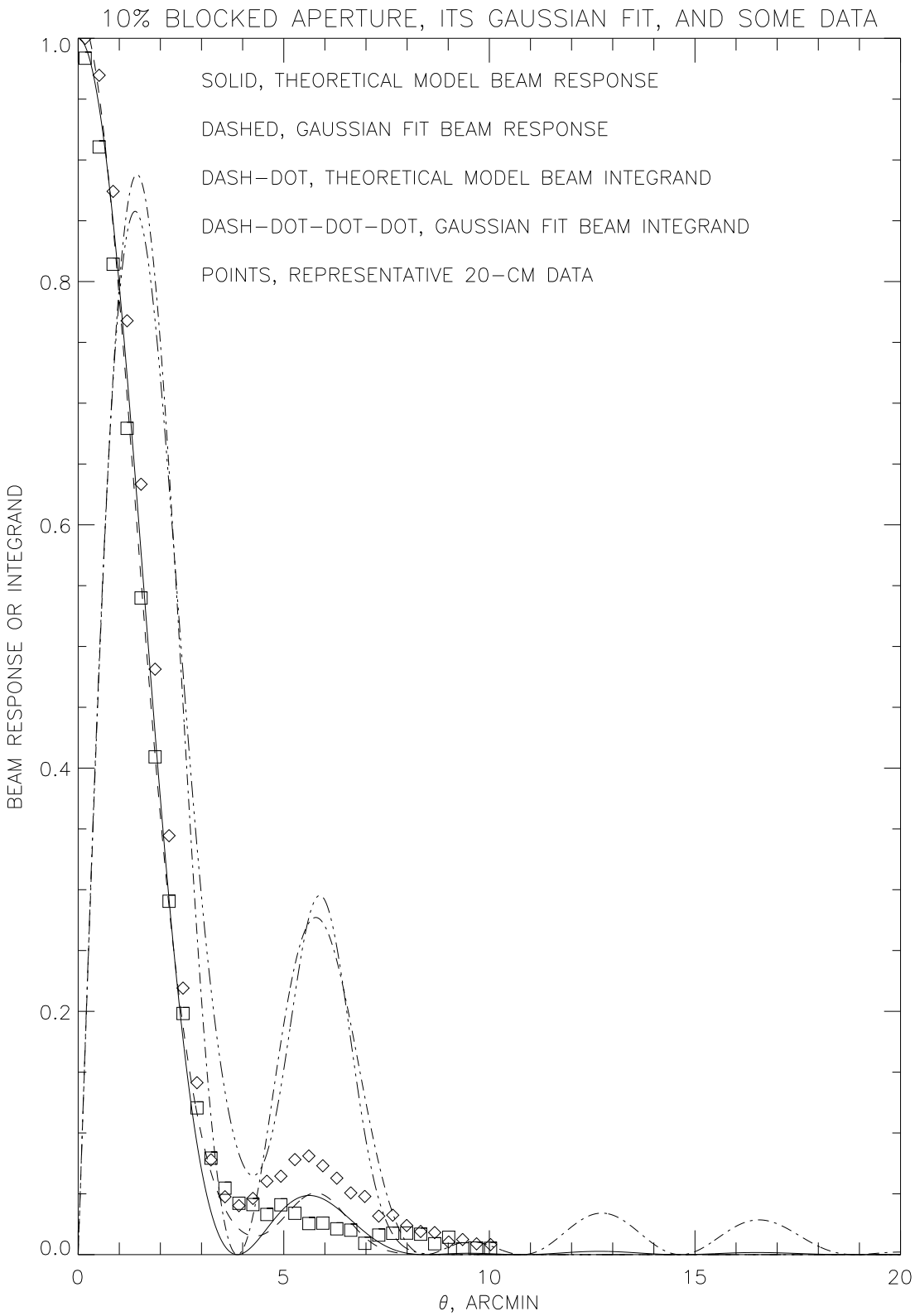
10% BLOCKED APERTURE, ITS GAUSSIAN FIT, AND SOME DATA
SOLID, THEORETICAL MODEL BEAM RESPONSE
DASHED, GAUSSIAN FIT BEAM RESPONSE
DASH–DOT, THEORETICAL MODEL BEAM INTEGRAND
DASH–DOT–DOT–DOT, GAUSSIAN FIT BEAM INTEGRAND
POINTS, REPRESENTATIVE 20–CM DATA
BEAM RESPONSE OR INTEGRAND
1.0
0.8
0.6
0.4
0.2
0.0
0
5
10
15
20
θ, ARCMIN

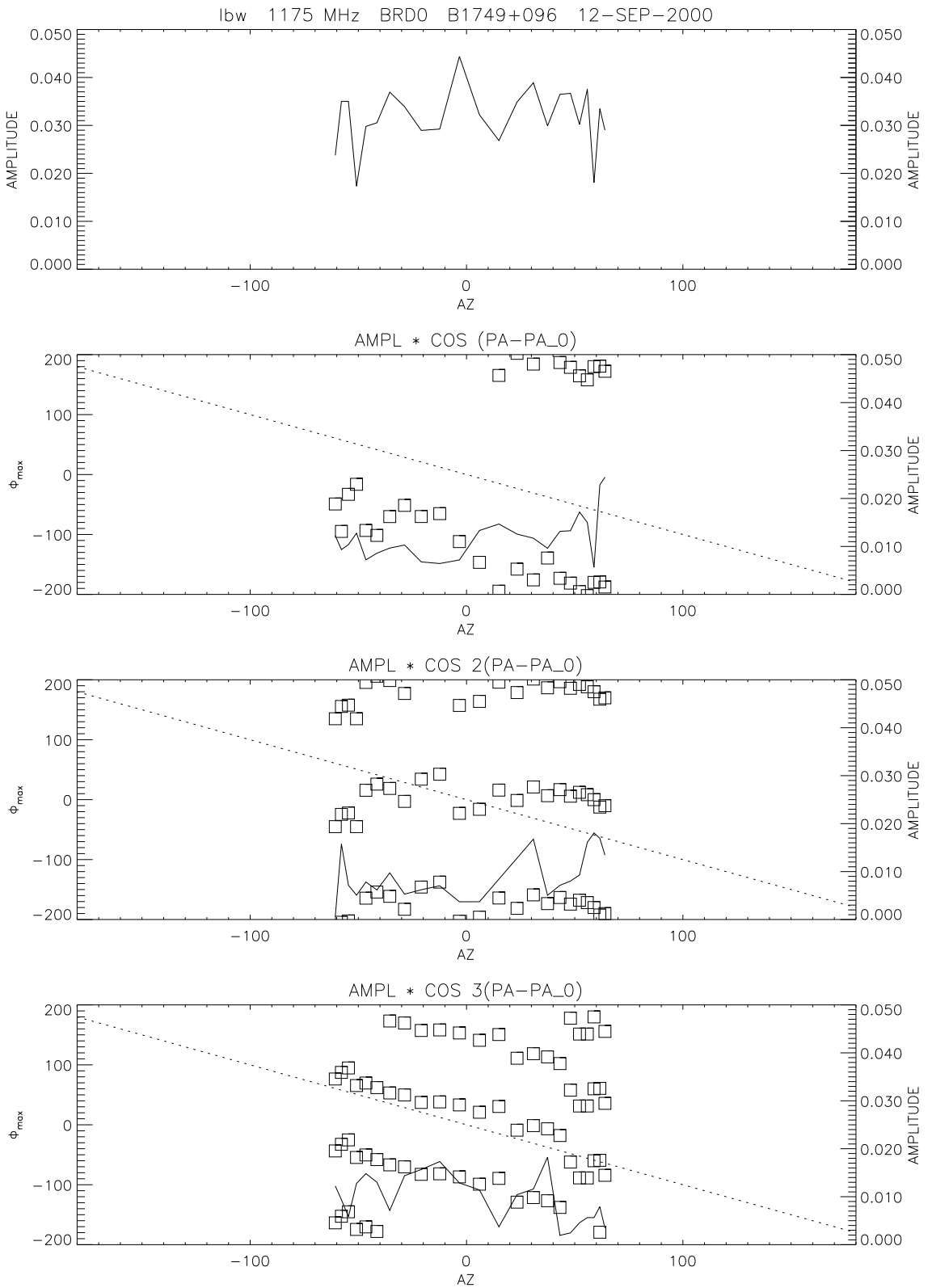
lbw 1175 MHz BRD0 B1749+096 12-SEP-2000
AMPLITUDE
AZ
AMPL * COS (PA-PA_0)
Φ_{max}
AMPL * COS 2(PA-PA_0)
AMPL * COS 3(PA-PA_0)

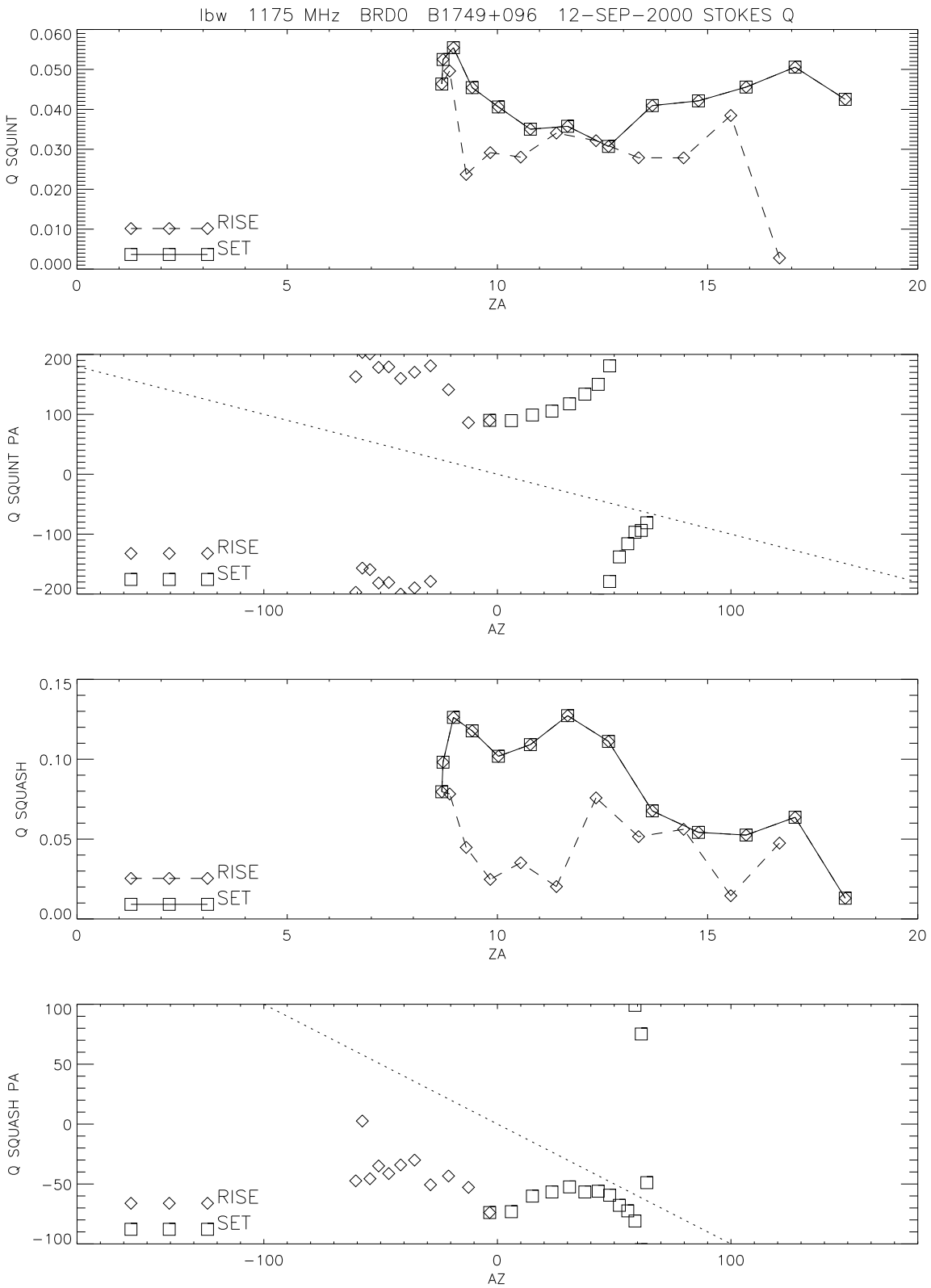
lbw 1175 MHz BRD0 B1749+096 12-SEP-2000 STOKES Q
Q SQUINT
0.060
0.050
0.040
0.030
0.020
0.010
0.000
RISE
SET
0
5
10
15
20
ZA
Q SQUINT PA
200
100
0
−100
−200
RISE
SET
−100
0
100
AZ
Q SQUASH
0.15
0.10
0.05
0.00
RISE
SET
0
5
10
15
20
ZA
Q SQUASH PA
100
50
0
−50
−100
RISE
SET
−100
0
100
AZ

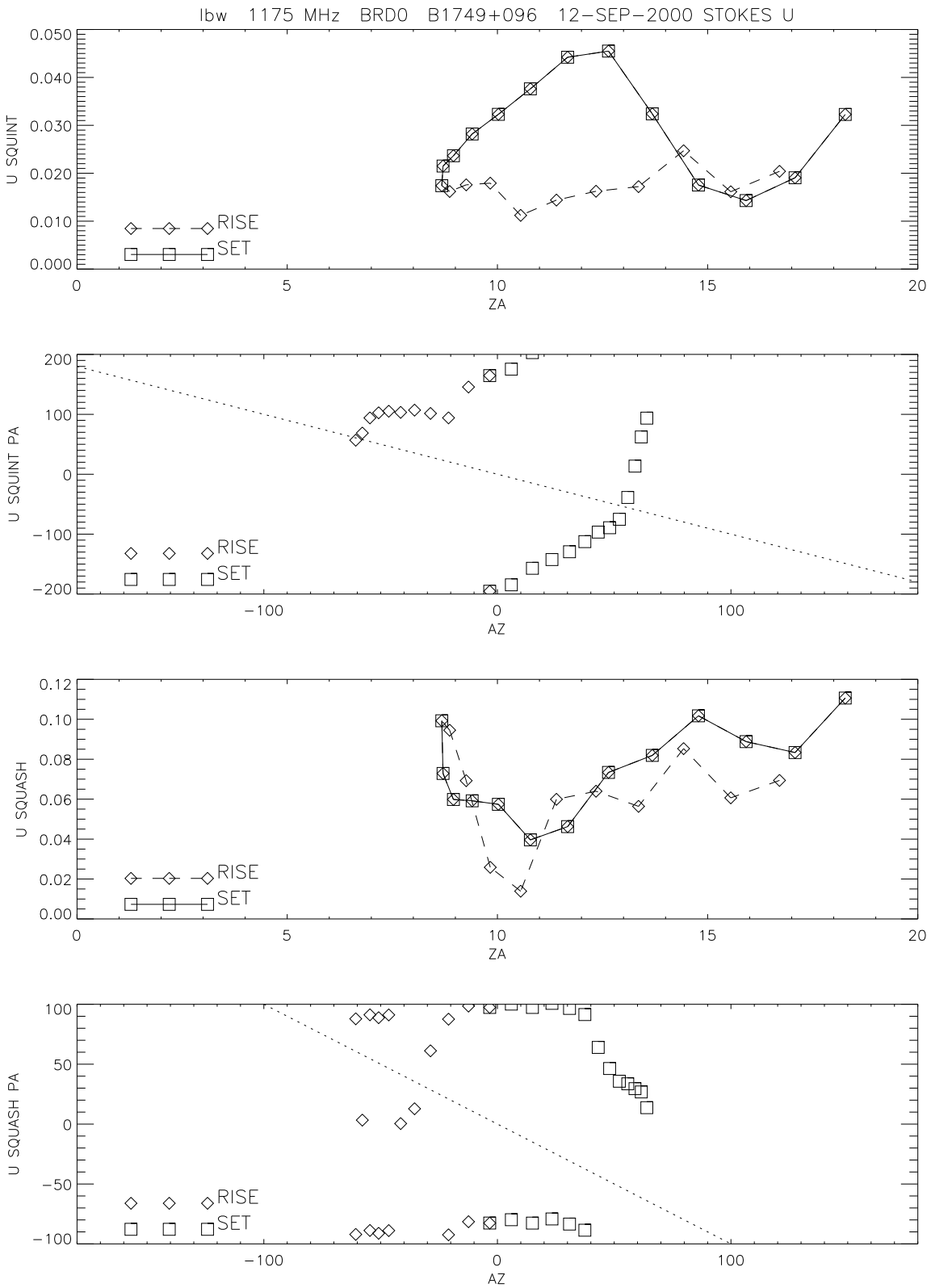
lbw 1175 MHz BRD0 B1749+096 12−SEP−2000 STOKES U
U SQUINT
0.050
0.040
0.030
0.020
0.010
0.000
0
5
10
15
20
ZA
RISE
SET
U SQUINT PA
200
100
0
−100
−200
−100
0
100
AZ
RISE
SET
U SQUASH
0.12
0.10
0.08
0.06
0.04
0.02
0.00
0
5
10
15
20
ZA
RISE
SET
U SQUASH PA
100
50
0
−50
−100
−100
0
100
AZ
RISE
SET

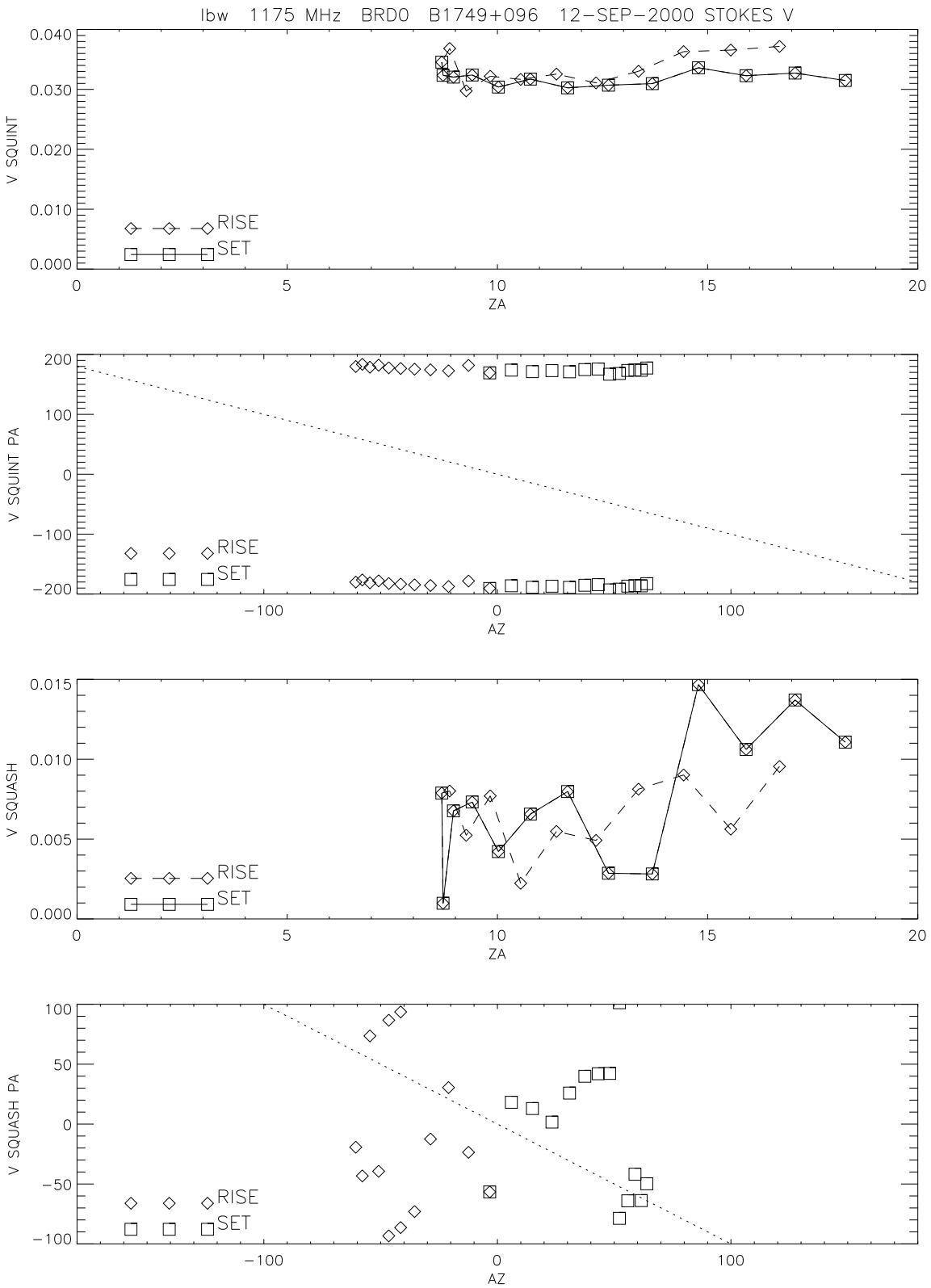
lbw 1175 MHz BRD0 B1749+096 12−SEP−2000 STOKES V
V SQUINT
0.040
0.030
0.020
0.010
0.000
RISE
SET
0
5
10
15
20
ZA
V SQUINT PA
200
100
0
−100
−200
RISE
SET
−100
0
100
AZ
V SQUASH
0.015
0.010
0.005
0.000
RISE
SET
0
5
10
15
20
ZA
V SQUASH PA
100
50
0
−50
−100
RISE
SET
−100
0
100
AZ

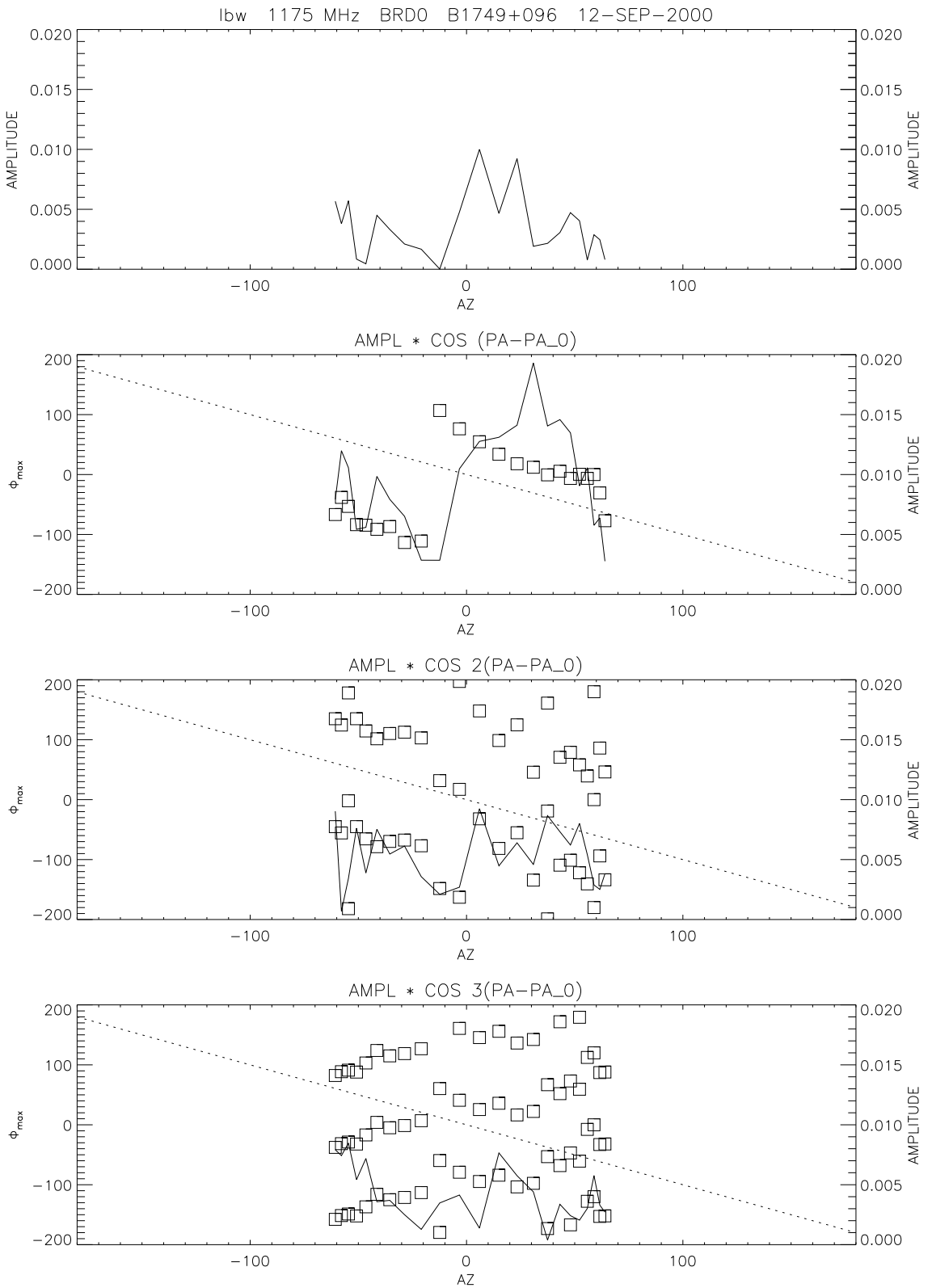
lbw 1175 MHz BRD0 B1749+096 12−SEP−2000
AMPLITUDE
AZ
AMPL * COS (PA−PA_0)
AMPL * COS 2(PA−PA_0)
AMPL * COS 3(PA−PA_0)
Φ_{max}

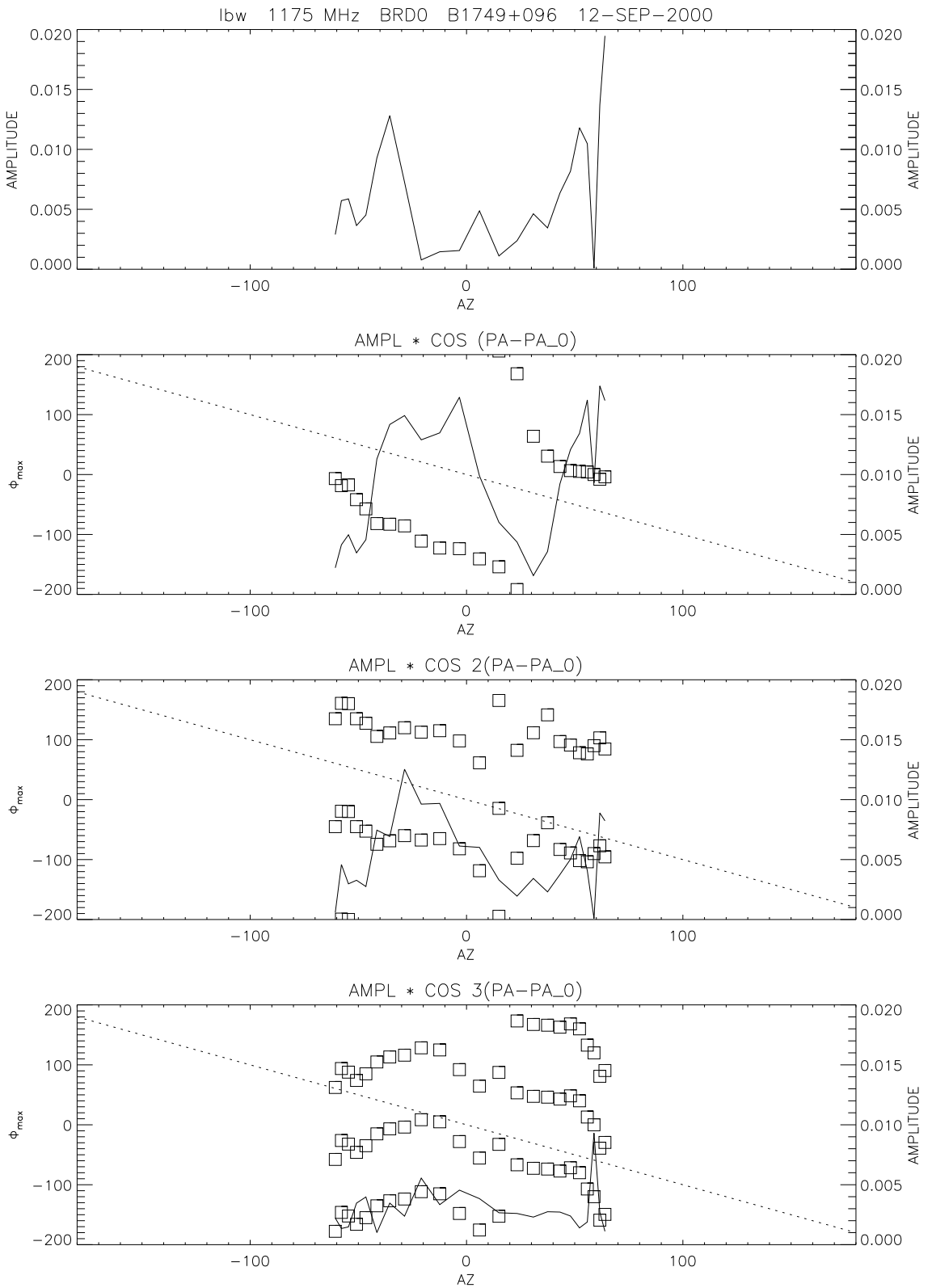
lbw 1175 MHz BRD0 B1749+096 12−SEP−2000
AMPLITUDE
AZ
AMPL * COS (PA−PA_0)
AMPL * COS 2(PA−PA_0)
AMPL * COS 3(PA−PA_0)
Φmax

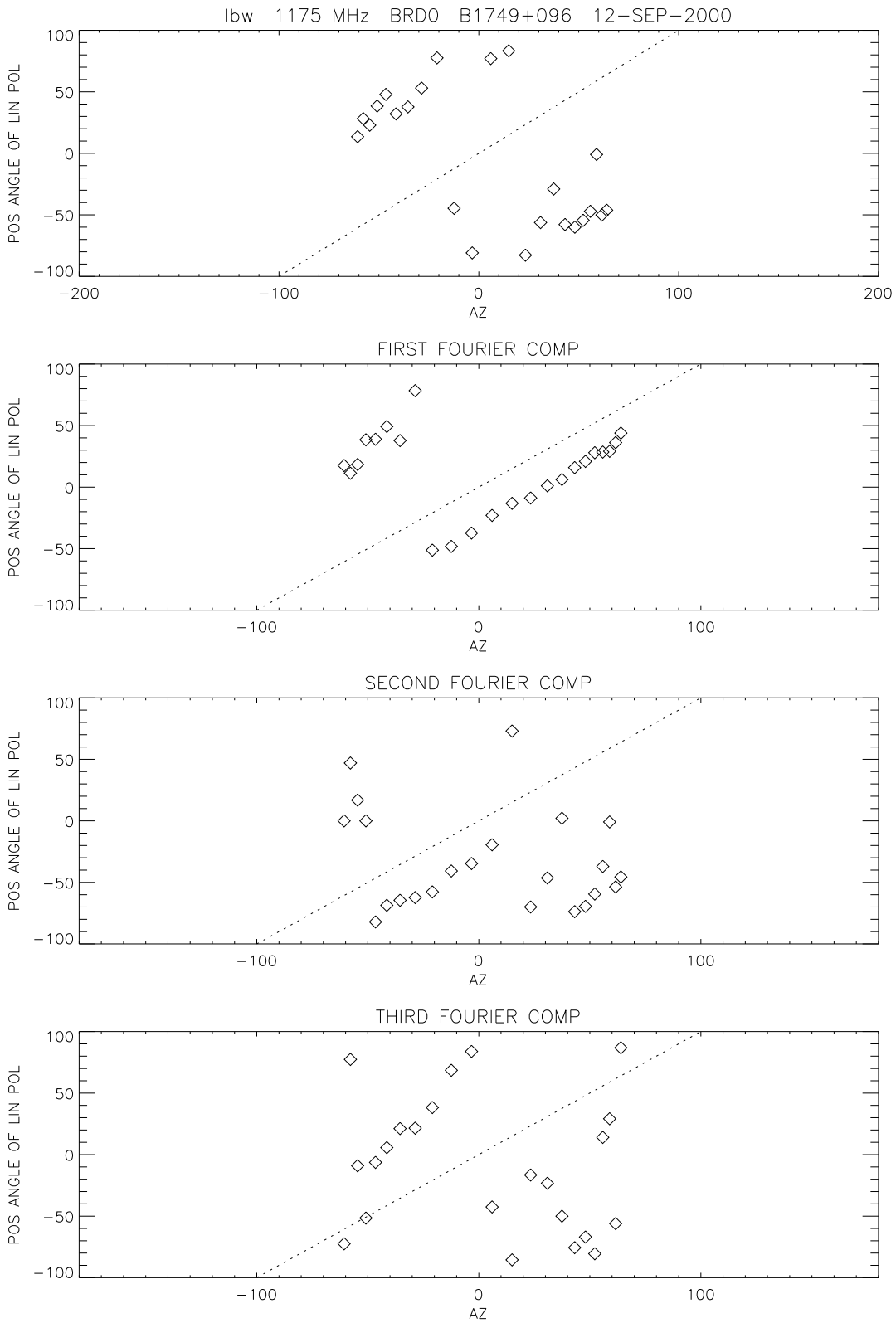
lbw 1175 MHz BRD0 B1749+096 12−SEP−2000
POS ANGLE OF LIN POL
AZ
FIRST FOURIER COMP
POS ANGLE OF LIN POL
AZ
SECOND FOURIER COMP
POS ANGLE OF LIN POL
AZ
THIRD FOURIER COMP
POS ANGLE OF LIN POL
AZ

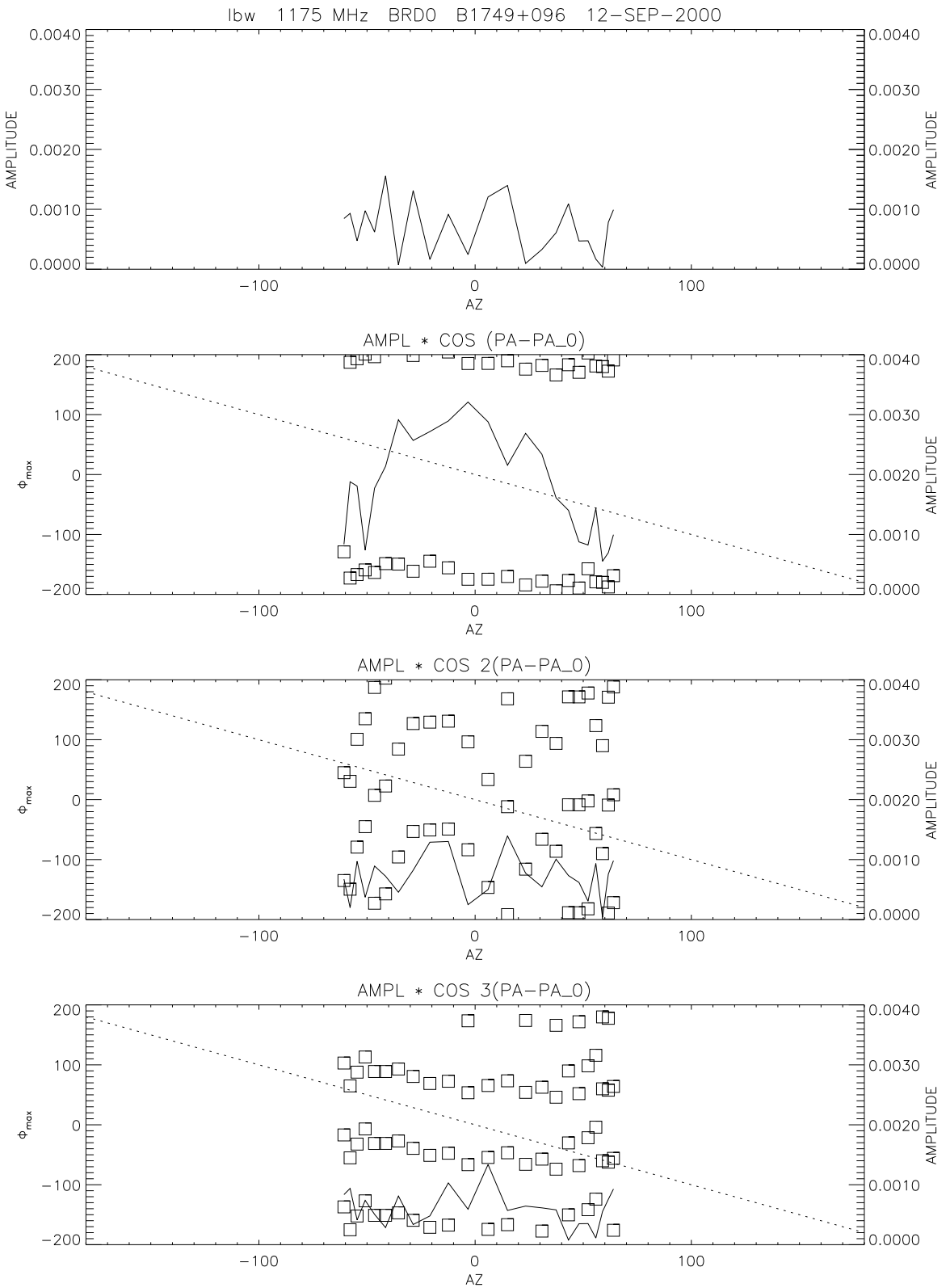
lbw 1175 MHz BRD0 B1749+096 12-SEP-2000
AMPLITUDE
AZ
AMPL * COS (PA-PA_0)
Φ_{max}
AMPL * COS 2(PA-PA_0)
AMPL * COS 3(PA-PA_0)

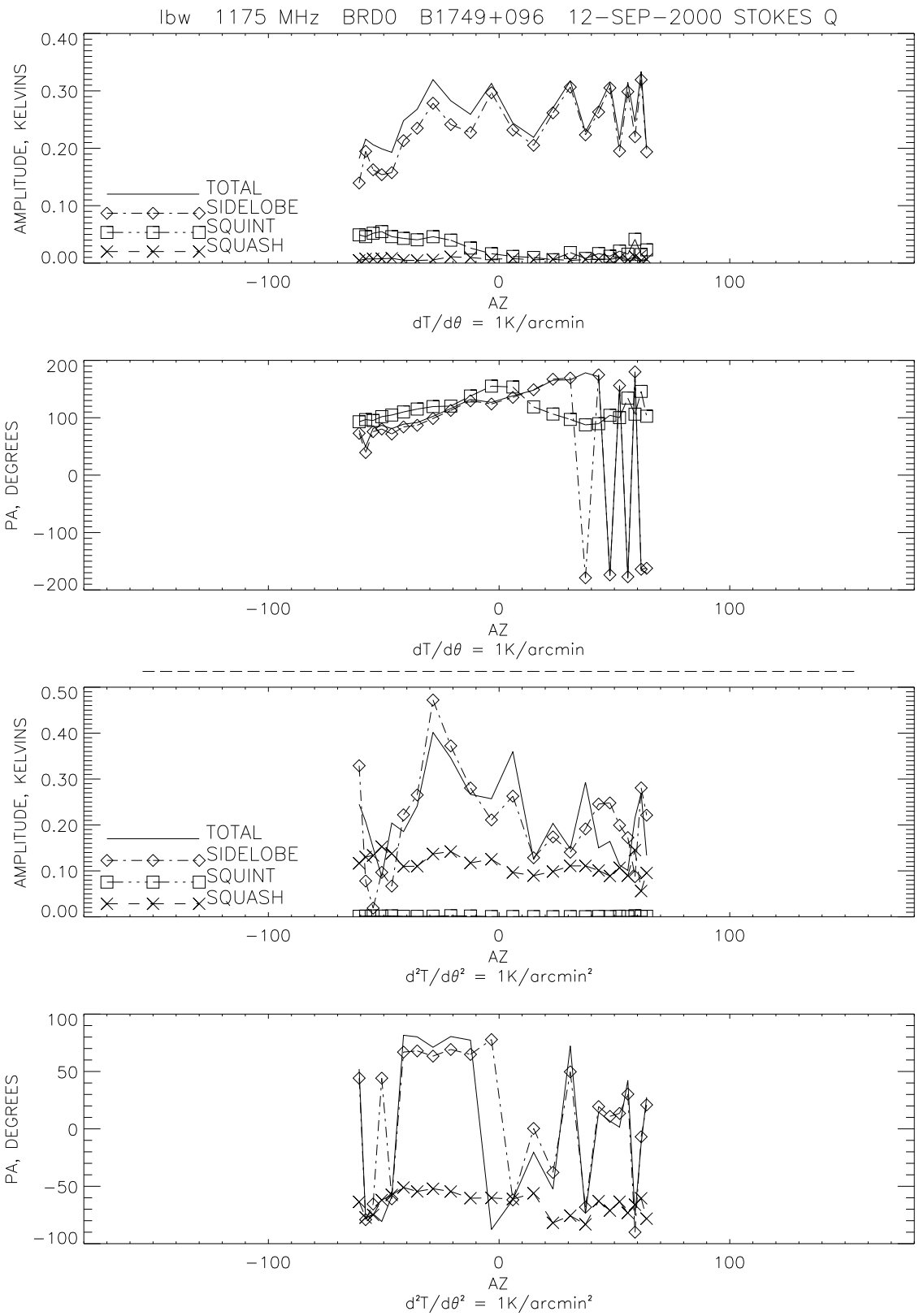
lbw 1175 MHz BRD0 B1749+096 12−SEP−2000 STOKES Q
AMPLITUDE, KELVINS
0.40
0.30
0.20
0.10
0.00
TOTAL
SIDELOBE
SQUINT
SQUASH
−100
0
100
AZ
dT/dθ = 1K/arcmin
PA, DEGREES
200
100
0
−100
−200
−100
0
100
AZ
dT/dθ = 1K/arcmin
AMPLITUDE, KELVINS
0.50
0.40
0.30
0.20
0.10
0.00
TOTAL
SIDELOBE
SQUINT
SQUASH
−100
0
100
AZ
d²T/dθ² = 1K/arcmin²
PA, DEGREES
100
50
0
−50
−100
−100
0
100
AZ
d²T/dθ² = 1K/arcmin²

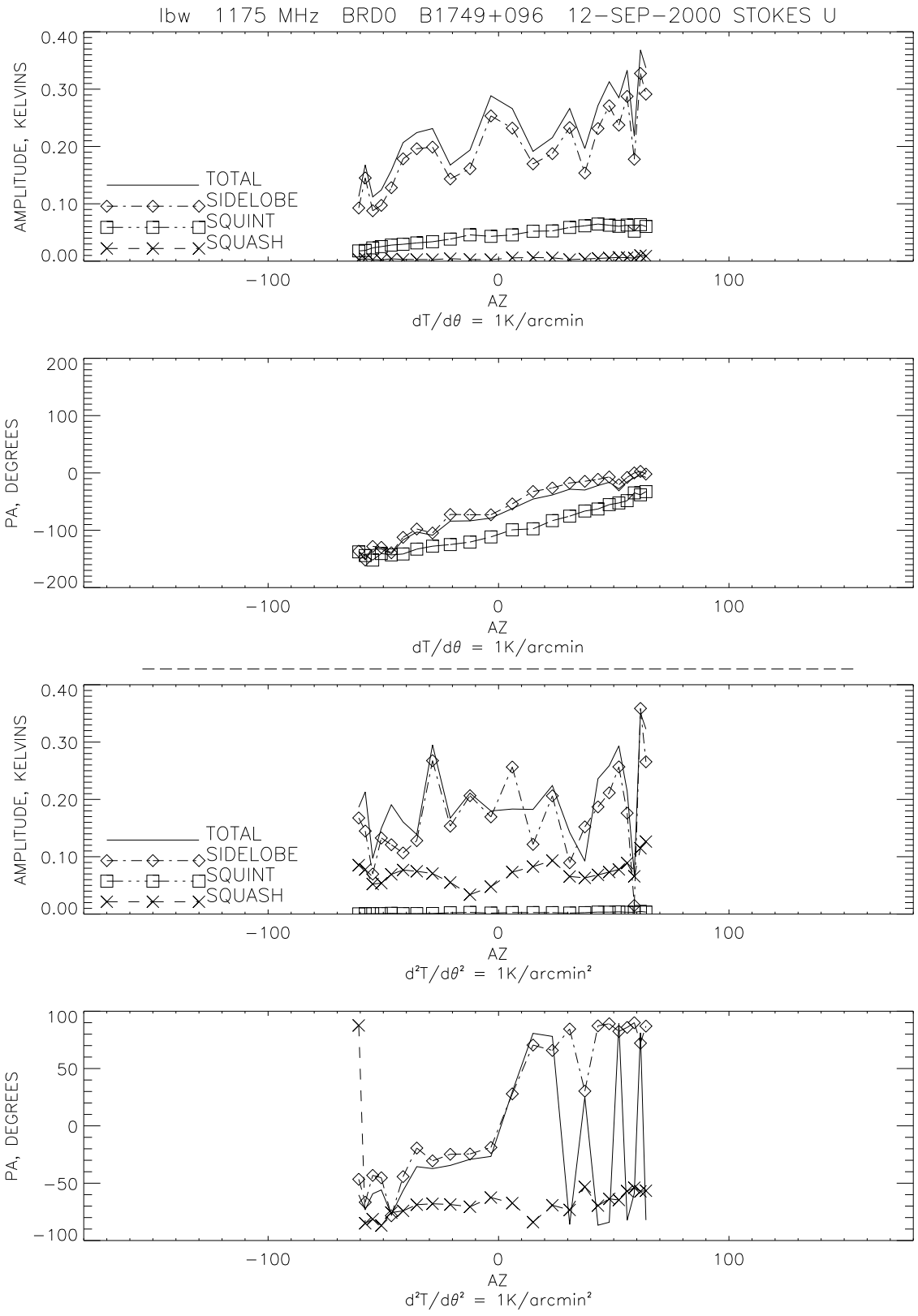
lbw 1175 MHz BRD0 B1749+096 12−SEP−2000 STOKES U
AMPLITUDE, KELVINS
0.40
0.30
0.20
0.10
0.00
TOTAL
SIDELOBE
SQUINT
SQUASH
−100
0
100
AZ
dT/dθ = 1K/arcmin
PA, DEGREES
200
100
0
−100
−200
−100
0
100
AZ
dT/dθ = 1K/arcmin
AMPLITUDE, KELVINS
0.40
0.30
0.20
0.10
0.00
TOTAL
SIDELOBE
SQUINT
SQUASH
−100
0
100
AZ
d²T/dθ² = 1K/arcmin²
PA, DEGREES
100
50
0
−50
−100
−100
0
100
AZ
d²T/dθ² = 1K/arcmin²

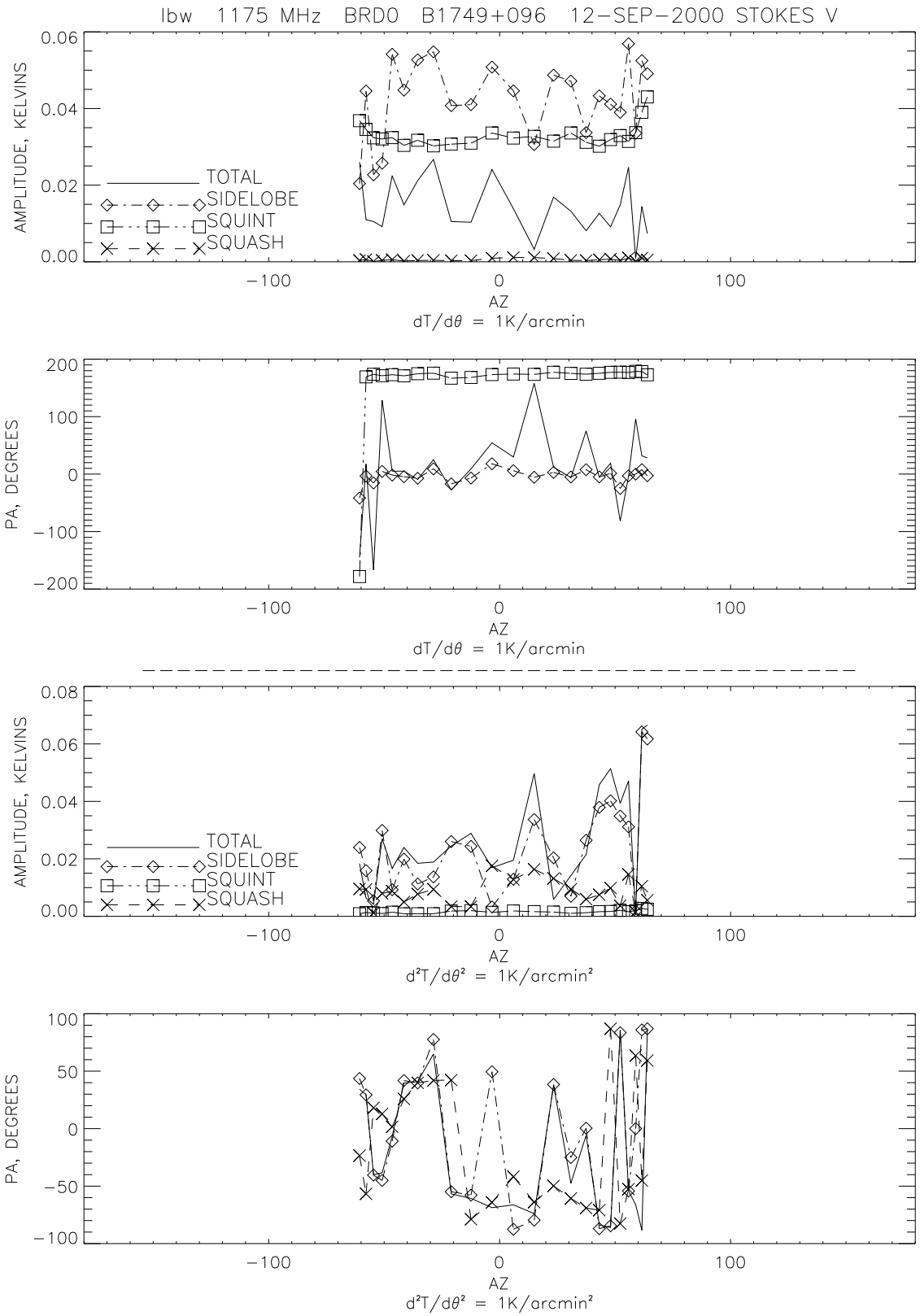
Ibw 1175 MHz BRD0 B1749+096 12−SEP−2000 STOKES V
AMPLITUDE, KELVINS
0.06
0.04
0.02
0.00
TOTAL
SIDELOBE
SQUINT
SQUASH
−100
0
100
AZ
dT/dθ = 1K/arcmin
PA, DEGREES
200
100
0
−100
−200
−100
0
100
AZ
dT/dθ = 1K/arcmin
AMPLITUDE, KELVINS
0.08
0.06
0.04
0.02
0.00
TOTAL
SIDELOBE
SQUINT
SQUASH
−100
0
100
AZ
d²T/dθ² = 1K/arcmin²
PA, DEGREES
100
50
0
−50
−100
−100
0
100
AZ
d²T/dθ² = 1K/arcmin²

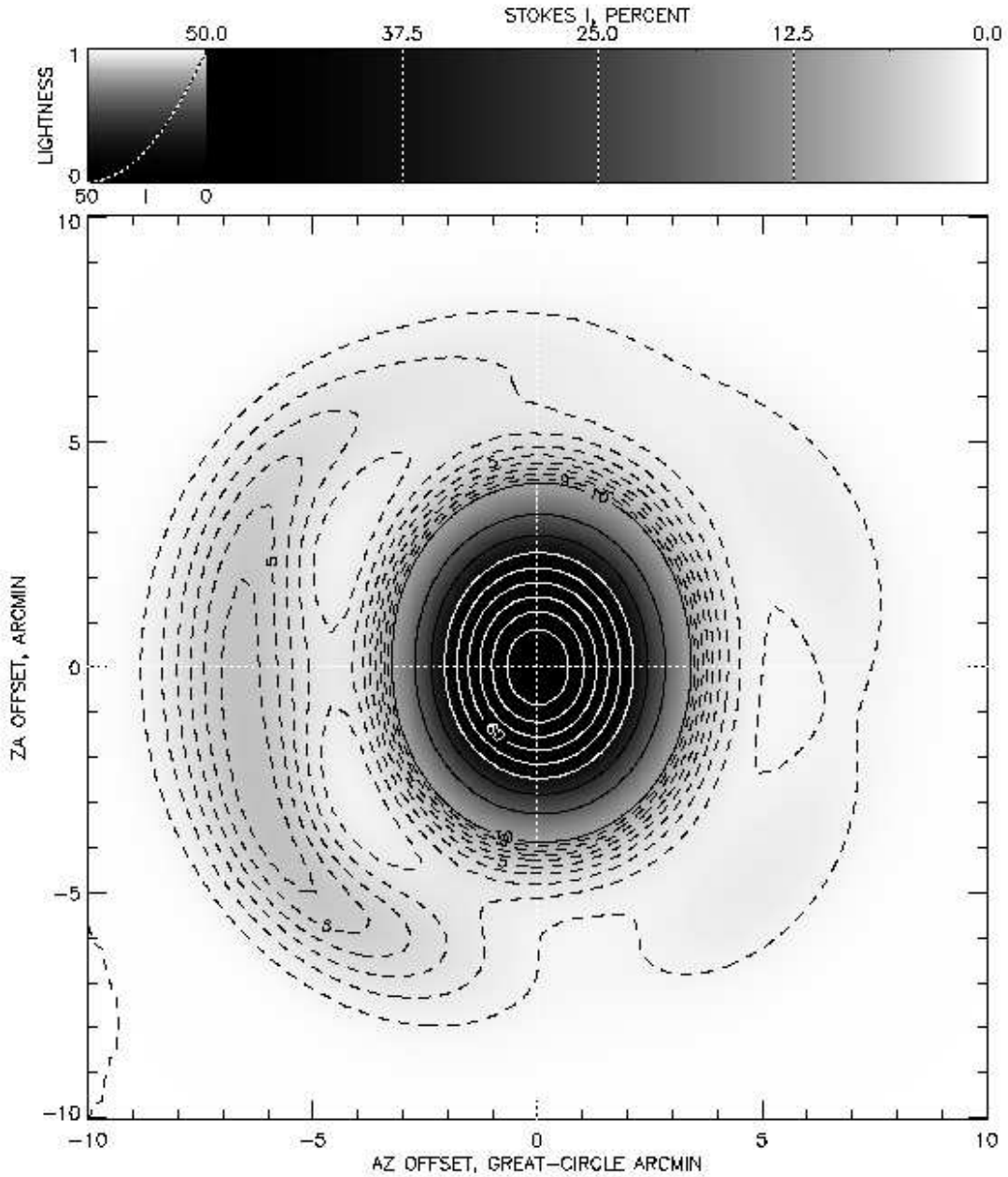
STOKES I, PERCENT
50.0
37.5
25.0
12.5
0.0
LIGHTNESS
1
0
50
I
0
10
5
0
−5
−10
ZA OFFSET, ARCMIN
−10
−5
0
5
10
AZ OFFSET, GREAT−CIRCLE ARCMIN

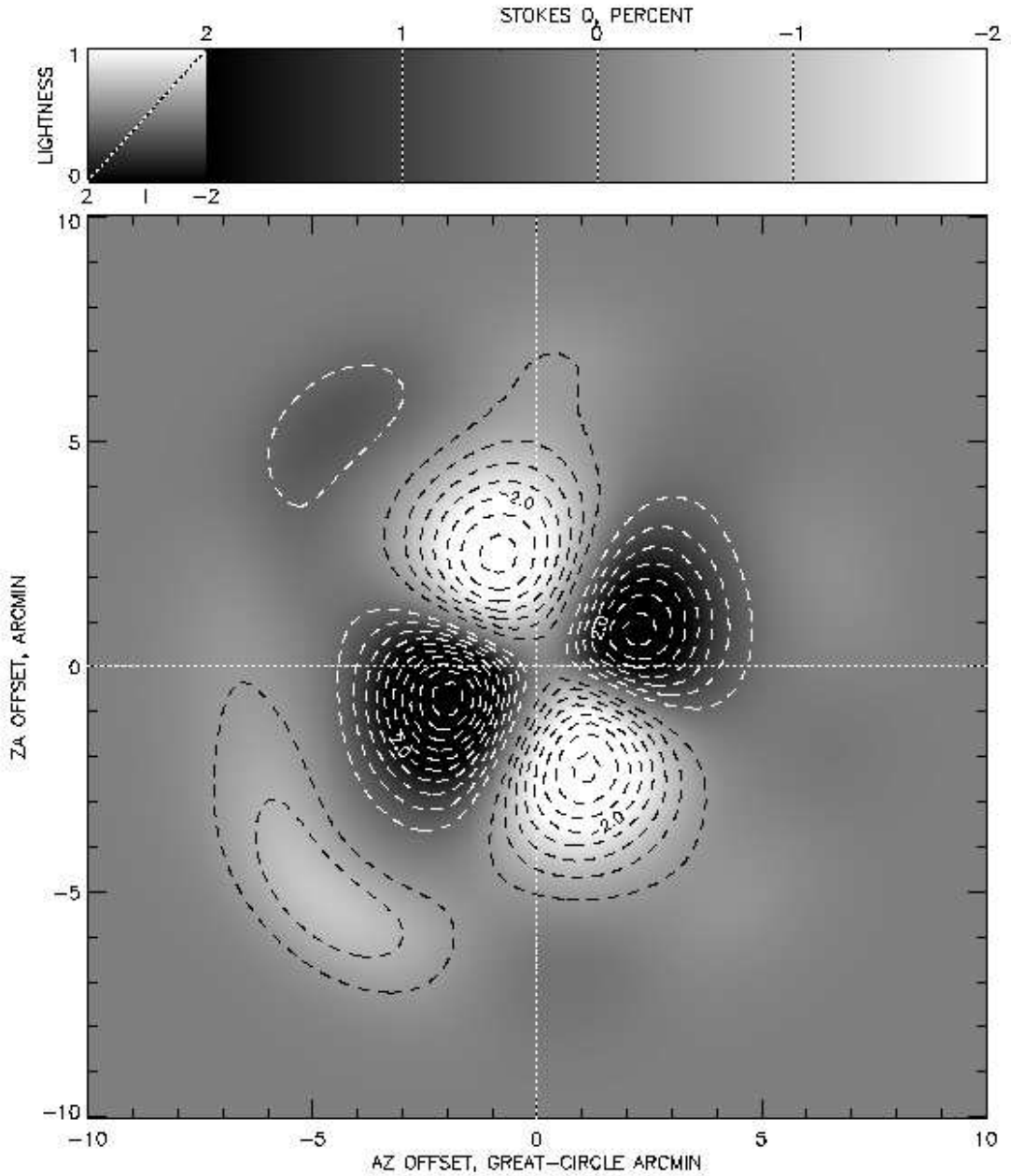
STOKES Q, PERCENT
2
1
0
−1
−2
LIGHTNESS
1
0
2
1
−2
10
5
0
−5
−10
ZA OFFSET, ARCMIN
2.0
2.0
2.0
2.0
−10
−5
0
5
10
AZ OFFSET, GREAT−CIRCLE ARCMIN

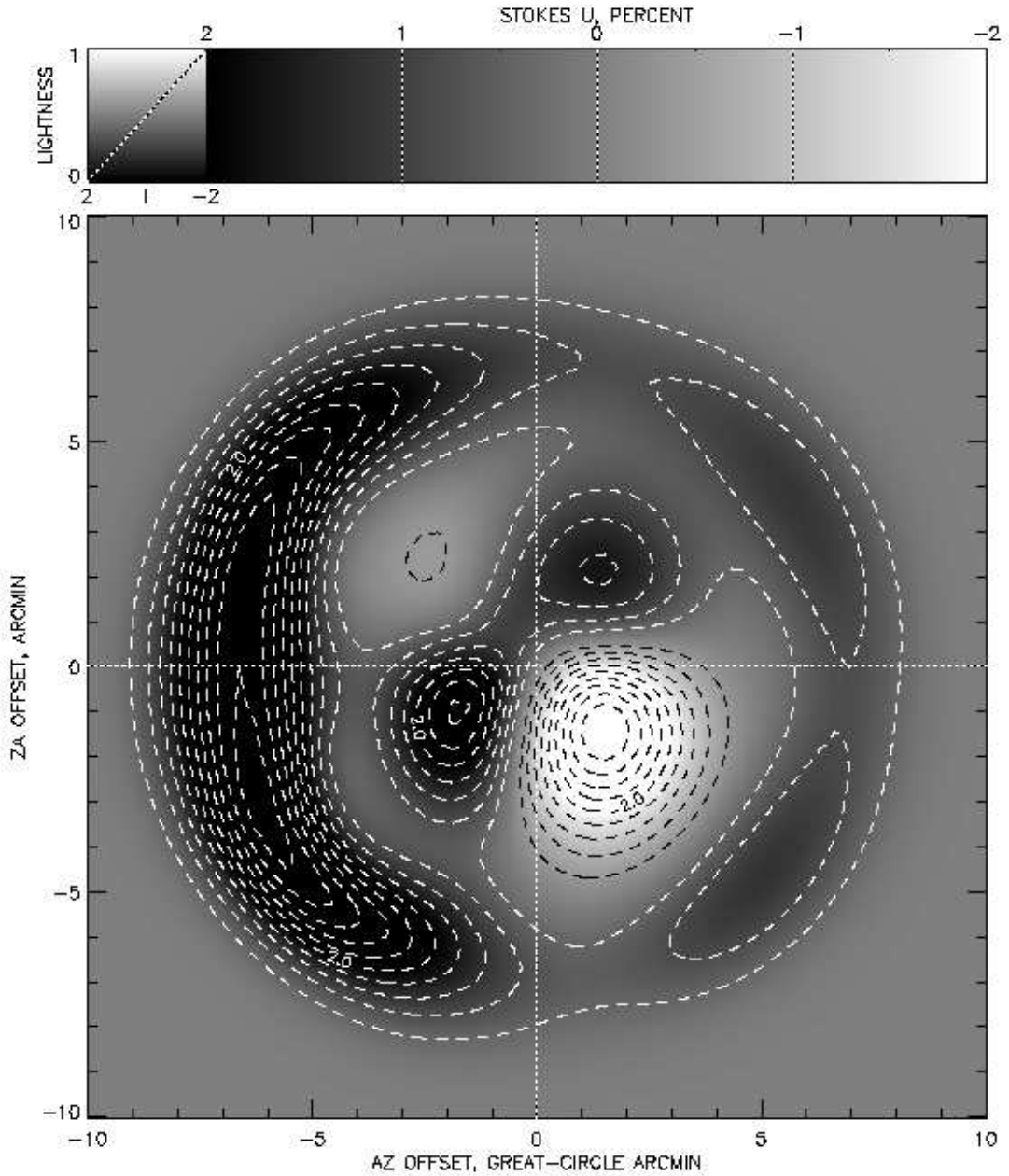
STOKES U, PERCENT
2
1
0
−1
−2
LIGHTNESS
1
0
2
1
−2
10
5
0
−5
−10
2.0
1.0
−1.0
−2.0
ZA OFFSET, ARCMIN
−10
−5
0
5
10
AZ OFFSET, GREAT−CIRCLE ARCMIN

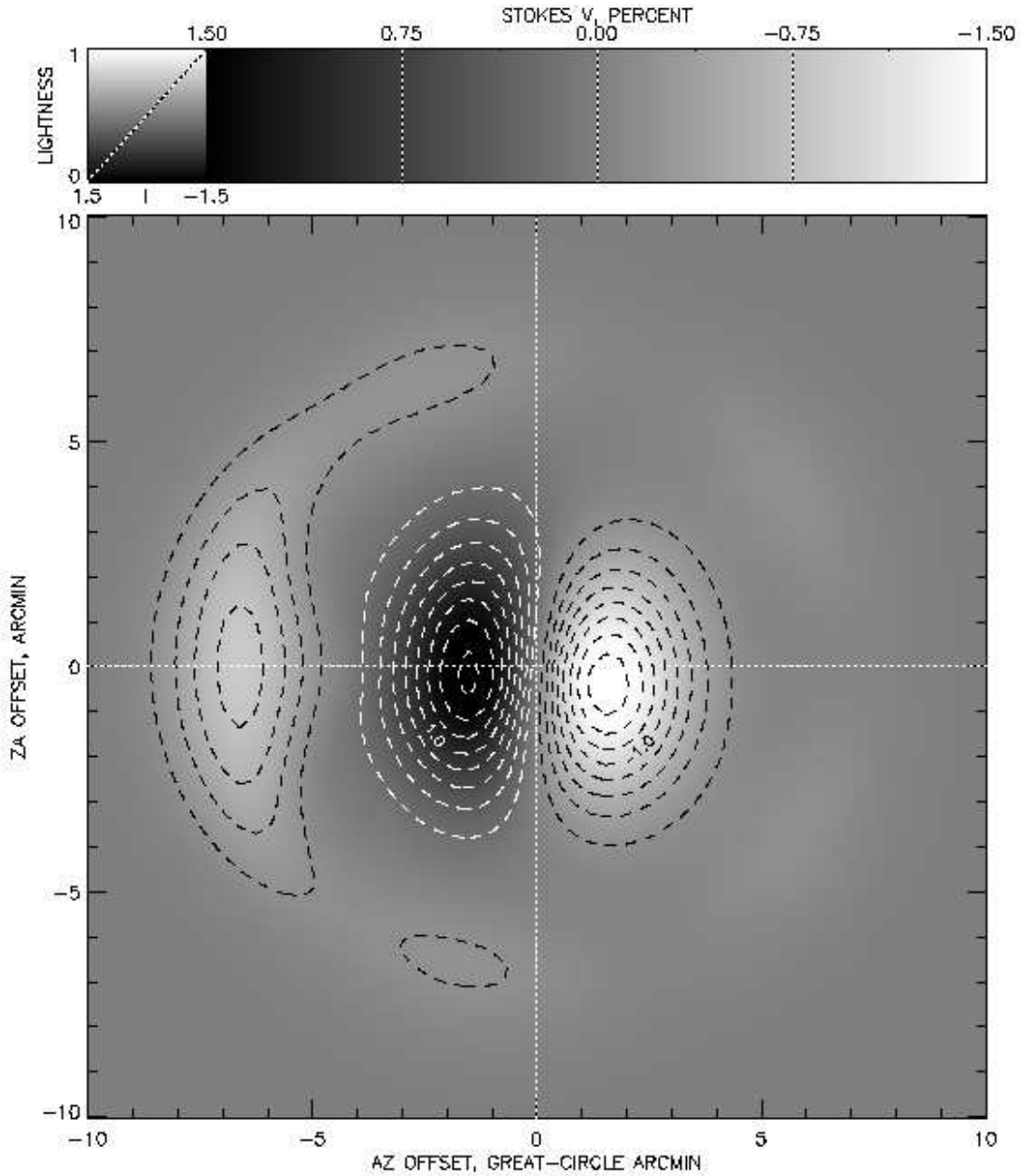
STOKES V, PERCENT
1.50
0.75
0.00
−0.75
−1.50
LIGHTNESS
1
0
1.5
I
−1.5
10
5
0
−5
−10
ZA OFFSET, ARCMIN
−10
−5
0
5
10
AZ OFFSET, GREAT−CIRCLE ARCMIN